STUDIES FOR CESR-TA: A LOW-EMITTANCE TEST ACCELERATOR AT THE CORNELL ELECTRON STORAGE RING

A Dissertation

Presented to the Faculty of the Graduate School

of Cornell University

in Partial Fulfillment of the Requirements for the Degree of

Doctor of Philosophy

by

Richard W. Helms

January 2008

STUDIES FOR CESR-TA: A LOW-EMITTANCE TEST ACCELERATOR AT

THE CORNELL ELECTRON STORAGE RING

Richard W. Helms, Ph.D.

Cornell University 2008

The International Linear Collider (ILC) is a proposed facility for studying collisions of electrons and positrons at $500\,\mathrm{GeV}$ (center of mass). The quality of the ILC's results will depend on its ability to reach the specified luminosity of $2\times10^{32}\,\mathrm{cm}^{-2}/\mathrm{s}$. Damping rings provide the required low-emittance beams, but the specifications for the ILC damping rings are ambitious by current standards. Important questions regarding dynamic instabilities need to be answered before the ILC design is finalized.

The CESR Test Accelerator (CesrTA) plan would convert the Cornell Electron Storage Ring into a low-emittance damping ring with parameters comparable to the ILC damping ring. However, achieving those parameters requires understanding and compensation for the magnet misalignments that increase vertical emittance.

We present calculations and simulations that characterize misalignments based on currently available survey data, and show that the two are consistent. We describe an algorithm for compensating for the misalignments, and optimize the parameters of that algorithm for various levels of misalignment and beam detector resolution. The corrected vertical emittance is less than the $10\,\mathrm{pm}$ target of the CesrTA proposal.

We optimize the same correction algorithm for the ILC damping ring, and show that, for CESR-level misalignments and detector performance, we also achieve the desired vertical emittance of 2 pm.

Finally, we describe a new way of measuring dispersion at CESR (and potentially at the ILC) using RF phase-modulation and multi-turn orbit measurements. This technique is faster than the current technique used at CESR, and our measurements show that the dispersion measured with the two techniques are in agreement with one another.

BIOGRAPHICAL SKETCH

Richard Ward Helms was born on August 21, 1977, in Parsons, Kansas. He attended public schools in Parsons, and later, in Nashville, Tennessee, graduating from Martin Luther King Magnet High School in 1996.

Richard remained in Nashville to attend Vanderbilt University, receiving his B.S. in physics in 2000. That year, he entered the doctoral program in physics at Cornell University, receiving his Ph.D. in 2008.

To my parents.

ACKNOWLEDGEMENTS

Mike Forster provided many useful discussions over the years of the practical aspect of CESR operations.

I was fortunate to have Jeremy Urban and Jeff Smith as officemates and friends. We worked on similar projects, attended countless meetings together, went to conferences together, and spent a lot of time bantering about every topic imaginable. When I think of my time as an accelerator physics student, I will always think of those two, as well.

Part of what made Cornell so rewarding was the quality of my classmates. Dan Johnson, Greg Maskel, Marko Nanias, Matt Shepherd, and Mark Wyman were (and are) the very best.

In my second year at Cornell, I was fortunate to find my way onto the Codes and Judicial Committee. Over the next few years, the CJC would have a profound impact on my decision to go to law school. Thanks go especially to Kathleen Rourke, who encouraged me to become chair of the committee, and to Mary Beth Grant and Linda Falkson, for their all their help.

My last two years at Vanderbilt were spent working in the group of Profs. Will Johns, Paul Sheldon, and Med Webster. They were an enormous part of my undergraduate education, and continue to be there for me.

Words cannot express the gratitude I feel toward my family. Everything I have achieved is a reflection of their love and support.

TABLE OF CONTENTS

LIST OF TABLES

LIST OF FIGURES

Chapter 1
Introduction

The CESR Test Accelerator (CesrTA) is a conversion of the Cornell Electron Storage Ring (CESR) from a high-luminosity collider to a low-emittance damping ring. Studies at CesrTA will help answer important questions about the design and operation of damping rings in the International Linear Collider (ILC).

This dissertation focuses on low-emittance tuning, i.e., compensating for those imperfections in a physical machine that increase the emittance. We are primarily concerned with CesrTA, but the techniques developed here are also directly applicable to the ILC.

1.1   Outline

In this introduction, we provide an overview of the ILC. We then describe CesrTA and how it will address damping ring issues.

In Chapter 2, we derive basic expressions for emittance and show analytically how emittance is impacted by machine imperfections.

In Chapter 3, we describe the expected level of magnet misalignment in CesrTA, and simulate the emittance.

In Chapter 4, we describe an algorithm for low-emittance tuning, and optimize the parameters in that algorithm to minimize the vertical emittance in CesrTA.

In Chapter 5, we apply the low-emittance tuning algorithm to the ILC, and describe it in the context of other possible ILC strategies.

In Chapter 6, we describe a new, faster method of measuring dispersion for CESR, and potentially, for the ILC. We present experimental results and compare them with those of the current measurement technique.

1.2 The International Linear Collider

1.2.1 Physics Goals

In 2008, the Large Hadron Collider (LHC) will begin operation, eventually reaching a collision energy of 14 TeV. The LHC will extend our view into the so-called *Terascale* with the expectation of profound discoveries, most notably, the long-anticipated observation of the Higgs boson [1, 2].

The ILC is a successor to the LHC. Although the ILC has discovery potential, it is usually thought of as a complimentary facility to the LHC, taking the LHC's discoveries and quantifying them with greater precision.

For example, although a light Higgs may be observed at the LHC, e^+e^- collisions allow the measurement of many different decay modes and branching ratios. Also, while the LHC may discover the existence of supersymmetric particles, measurements at the ILC environment are better suited for identifying the parameters of the underlying theory [3].

More general examples of LHC/ILC complementarity are shown in Table 1.1.

1.2.2 ILC Design

The ILC uses two superconducting linear accelerators to accelerate and collide electrons and positrons. Figure 1.1 shows the overall layout of the ILC. The two

Table 1.1: Complementarity of the LHC and ILC capabilities. [4]

If LHC discovers:	What ILC could do:
A Higgs particle	Discover why the Higgs exists and who its cousins are. Discover effects of extra dimensions or a new source of matter-antimatter asymmetry.
Superpartner particles	Detect the symmetry of supersymmetry. Reveal the supersymmetric nature of dark matter. Discover force unification and matter unification at ultra-high energies.
Evidence for extra dimensions	Discover the number and shape of the extra dimensions. Discover which particles are travelers in extra dimensions, and determine their locations within them.
Missing energy from a weakly-interaction heavy particle	Discover its identity as dark matter. Determine what fraction of the total dark matter it accounts for.
Heavy charged particles that appear to be stable	Discover that these eventually decay into very weakly interacting particles. Identify these "super-WIMPs" as dark matter.
A Z-prime particle, representing a previously unknown force of nature	Discover the origin of the Z-prime. Connect this new force to the unification of quarks with neutrinos, of quarks with the Higgs, or with extra dimensions.
Superpartner particles matching the predictions of supergravity	Discover telltale effects from the vibrations of super-strings.
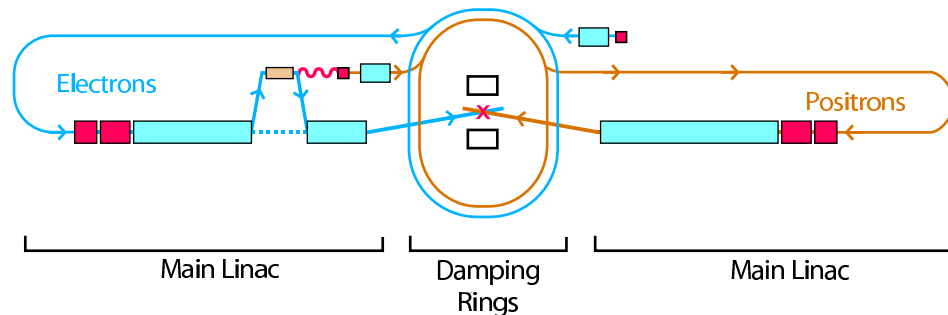
Figure 1.1: Diagram of the ILC complex. The electron and positron damping rings are shown around the interaction point.

most important design parameters are the center-of-mass energy of $500\,\mathrm{GeV}$, and the luminosity of $2 \times 10^{34}\,\mathrm{cm}^{-2}/\mathrm{s}$ [5]. Other parameters are shown in Table. 1.2.

The luminosity of a collider is given by

$$L = \frac{n_b\, N_e^2\, f}{4\pi\, \sigma_x^*\, \sigma_y^*} \times H_D \tag{1.1}$$

where n_b is the number of bunches, N_e is the number of particles per bunch, f is the pulse frequency, $\sigma_{x,y}^*$ are the horizontal and vertical beam sizes, and H_D is the disruption factor.

The vertical beam size depends on the vertical emittance ϵ_y and the vertical β-function. If we assume that $\beta_y^* = \sigma_z$ in order to minimize the hourglass effect, then we can write the luminosity as

$$L \approx 5.74 \times 10^{20}\,\mathrm{m} \times \frac{P_b}{E_{cm}} \times \sqrt{\frac{\delta_E}{\epsilon_y}} \times H_D \tag{1.2}$$

where P_b is the power in the beam, E_{cm} is the center-of-mass energy, and δ_E is the fractional beam energy loss due to beamstrahlung [6].

From Eq. 1.2, the best way to increase luminosity is to reduce the vertical emittance. That is accomplished by damping rings which reduce the phase-space volume of the beams through synchrotron radiation.

In ILC damping rings, the bunch train is wound around the damping rings several times, reducing the effective bunch spacing to a few nanoseconds. The short bunch spacing, together with the small vertical emittance, raises several performance issues that need to be addressed ahead of finalizing a design. The main goals of CesrTA are to study these damping ring issues in an environment that is a reasonable approximation to the ILC damping rings.

Table 1.2: ILC Parameters

Parameter	Value
Center-of-mass energy	$500\,\mathrm{GeV}$
Peak luminosity	$2\times10^{34}\,\mathrm{cm}^{-2}/\mathrm{s}$
Repetition rate	$5\,\mathrm{Hz}$
Main Linacs	
Average accelerating gradient	$31.5\,\mathrm{MV/m}$
Length of each Main Linac	$11\,\mathrm{km}$
Beam pulse length	$1\,\mathrm{ms}$
Total site length	$31\,\mathrm{km}$
Total site power consumption	$230\,\mathrm{MW}$
Total installed power	$300\,\mathrm{MW}$
Number of particles per bunch	2×10^{10}
Number of bunches per pulse	2625
Bunch interval in the Main Linac	$369.2\,\mathrm{ns}$
in units of RF buckets	480
Average beam current in pulse	$9.0\,\mathrm{mA}$
Normalized emittance at IP x	$10\,\mathrm{mm}\cdot\mathrm{mrad}$
Normalized emittance at IP y	$0.04\,\mathrm{mm}\cdot\mathrm{mrad}$
Beta function at IP x	$20\,\mathrm{mm}$
Beta function at IP y	$0.4\,\mathrm{mm}$
RMS beam size at IP x	$639\,\mathrm{nm}$
RMS beam size at IP y	$5.7\,\mathrm{nm}$
RMS bunch length z	$300\,\mathrm{\mu m}$
Crossing angle	$14\,\mathrm{mrad}$

1.3 CesrTA

1.3.1 CesrTA Goals

CesrTA will address a number of issues regarding the ILC damping rings, most have to do with low-emittance operation. These include the following [7]:

- Characterization of electron cloud build-up
- Development modeling tools for electron cloud instabilities
- Determination of electron cloud instability thresholds
- Characterization of ion effects
- Specification of techniques for suppressing ion effects.

The most critical issue for the positron damping ring is the electron cloud effect. This occurs when radiation from the beam strikes the vacuum chamber, causing the emission of photoelectrons. The beam then drives those electrons into the vacuum chamber, causing the emission of secondary electrons. If the number of emitted electrons grows sufficiently large, a so-called *electron cloud* forms and may disrupt the beam itself.

Measurements of the electron cloud have already been performed at CESR, but CesrTA will have the opportunity to study its impact on ultra low-emittance beams. CesrTA will also have the opportunity to evaluate suppression techniques such as chemical coating of the vacuum chamber, or grooved chambers [8].

In addition to low-emittance studies, CesrTA will provide the opportunity to test hardware and instrumentation for the ILC, including kickers, wigglers, and alignment and survey techniques.

1.3.2 CesrTA Design

CESR must be reconfigured in order to operate in the same emittance regime as the ILC damping rings. The CesrTA lattice creates three zero-dispersion regions and relocates the superconducting wigglers to those areas. The resulting lattice functions are shown in Fig. 1.2 and the parameters for CesrTA are shown in Table 1.3.

It is evident from Fig. 1.3 that CesrTA is significantly smaller than the ILC damping ring. Its energy is also lower ($2\,\text{GeV}$ vs. $5\,\text{GeV}$), however, CesrTA will be similar to the ILC damping rings in several important ways [9]:

CesrTA will be wiggler-dominated. Wigglers are a significant driver of non-linear behavior in damping rings, and are especially problematic in generating electron clouds. Understanding that behavior will be critical in ILC damping rings. CESR wigglers are well characterized, and will provide a baseline design for ILC wigglers [10].

CesrTA can store electrons or positrons. Some of the instabilities that will be of concern in the ILC (e.g., electron cloud) are species-dependent. CesrTA can study those phenomena and make a direct comparison between the different species.

CesrTA can operate with variable bunch-spacing. The nominal bunch spacing is $14\,\text{ns}$, but with upgrades, that can be reduced to as small as $2\,\text{ns}$. This will allow CesrTA to study multi-bunch instabilities that may impact the ILC.

CesrTA will have a vertical emittance comparable to the ILC. The emittance requirements for the ILC are beyond the capabilities of present storage rings. CesrTA will provide opportunities to study the effects of machine

β_x (m)

β_y (m)

η_x (m)

Longitudinal position (m)
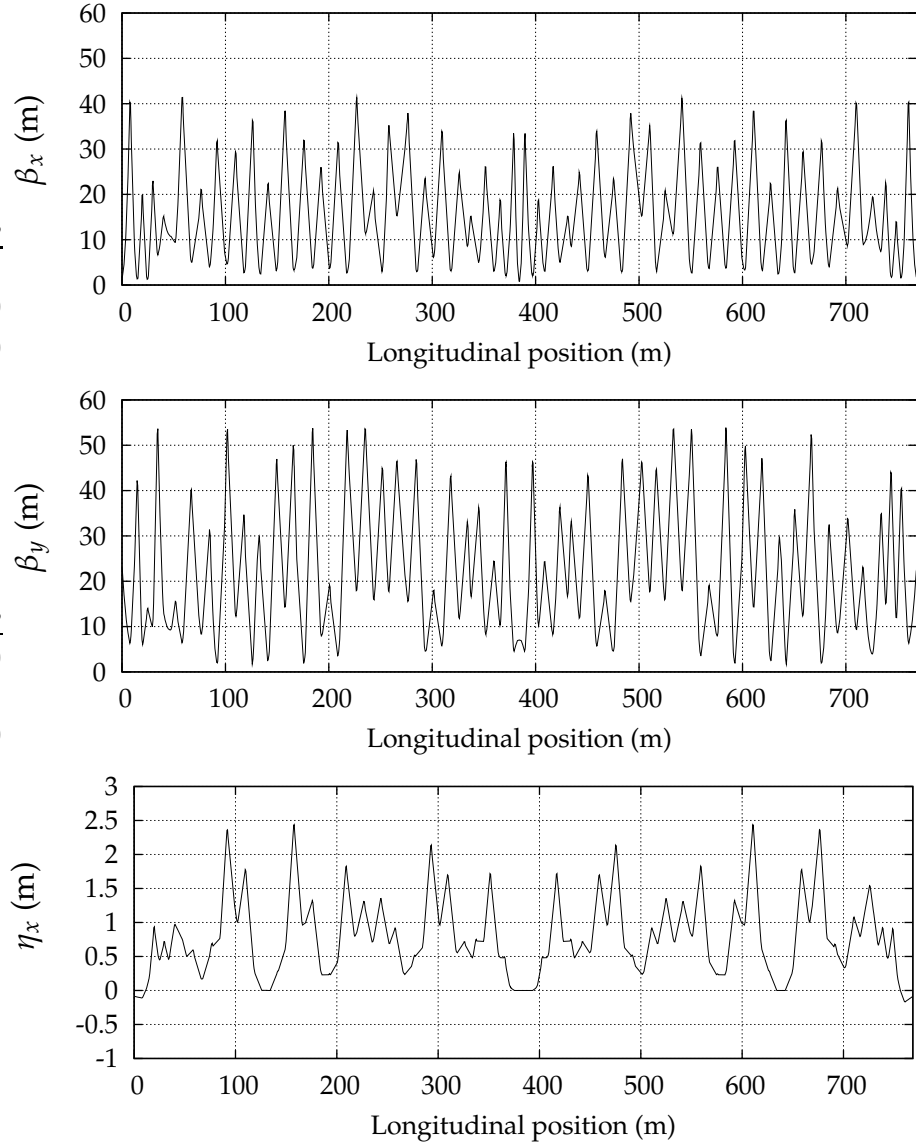
Figure 1.2: CesrTA lattice functions. Horizontal (top) and vertical (middle) β-functions, and horizontal dispersion (bottom) with three zero-dispersion regions for wigglers.

8
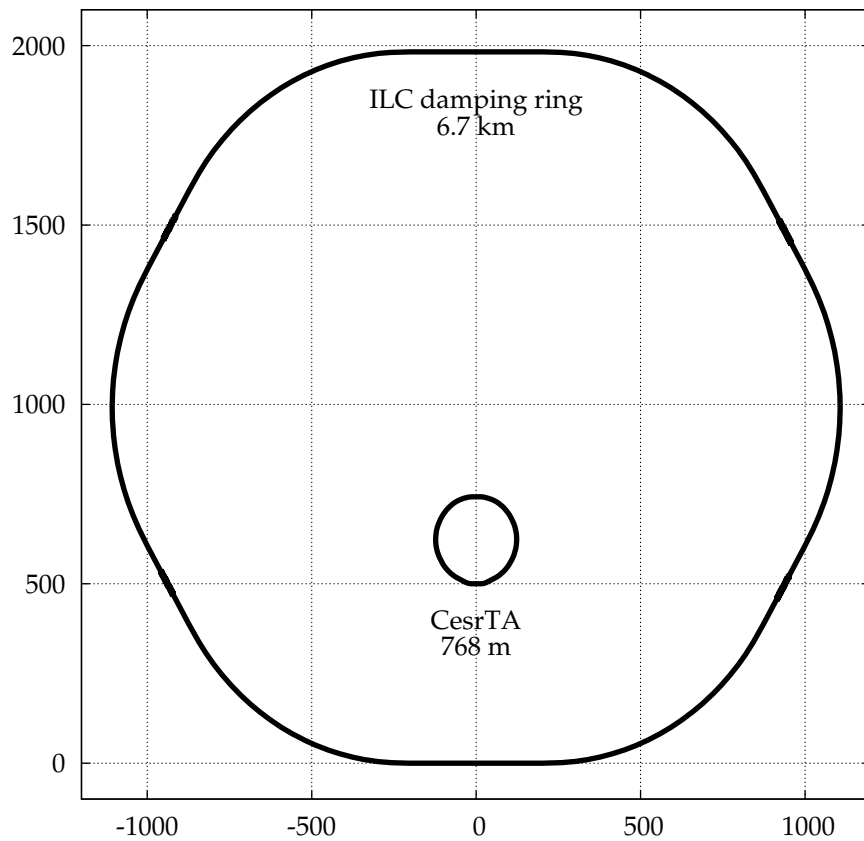
Figure 1.3: Relative size of CesrTA and the ILC damping ring. Scale is in meters.

imperfections and low-emittance tuning in the ILC regime, and emittance dilution due to the electron cloud and other collective effects.

The small horizontal emittance from the new lattice helps reduce the amount of vertical emittance due to coupling, but magnet misalignments are still present and must be corrected. In CesrTA this is accomplished by 62 vertical correctors (for correcting the orbit and dispersion) and 18 skew quadrupoles (for correcting the dispersion and coupling).

The vertical correctors are distributed uniformly throughout the ring. However, since the skew quadrupoles have previously been used to correct coupling from the CLEO solenoid, they are concentrated near the interaction point.

CESR has 99 beam position monitors, 13 of which have upgraded electronics and are capable of taking turn-by-turn measurements. The remaining BPMs will be upgraded for CesrTA.

This dissertation discusses sources of emittance dilution in the CesrTA lattice and beam-based techniques for minimizing the vertical emittance.

Table 1.3: CesrTA parameters.

Parameter	Value
Energy (GeV)	2.0
Circumference (m)	768.44
σ_E/E	8.6×10^{-4}
Bunch Length (mm)	18
Energy loss/turn (MeV)	0.22
Momentum compaction	1.0×10^{-3}
Horizontal emittance (nm)	3.3
Damping time (s)	
$\tau_{x,y}$ (s)	0.048
τ_x	0.024
Damping Partition number	
$\mathcal{J}_x$	0.999397
$\mathcal{J}_y$	1.000394
$\mathcal{J}_z$	2.000209
Tune/2π	
Q_x	14.530
Q_y	9.580
Chromaticity	
ξ_x	2.960
ξ_y	3.376
Mean $\beta_{x,y}$ (m)	15.496, 22.523
Mean η_x (m)	0.793

Chapter 2
Emittance in Damping Rings

2.1 Introduction

The remainder of this thesis is devoted to various aspects of generating low-emittance beams in damping rings. This chapter starts with the basic mathematical formulas that describe damping ring emittance. Those formulas are extended to include the effect of random element misalignments, which are the principle cause of vertical emittance.

Simulations are then used to arrive at a more realistic characterization of the vertical emittance in CesrTA, and those simulations are, where applicable, compared to analytic calculations.

Finally, sources of vertical emittance other than random misalignment are considered and shown to be negligible for the CesrTA design. We do not consider collective (current-dependent) effects.

2.2 Horizontal Emittance

Both the horizontal and vertical emittance depend largely on the dispersion function in that plane. For rings that lie in the horizontal plane, the horizontal dispersion is known reasonably well based on the design of the lattice. In contrast, the vertical dispersion is given by imperfections by which the physical ring differs from the design. Therefore, we start with a calculation of horizontal emittance, showing exactly where dispersion has an effect.

2.2.1 Analytic Calculation

Following mostly the treatment of [11] and [12], we begin with the definition of dispersion. In a ring, a particle with the design energy travels along a path that closes on itself after one turn, the so-called *on-energy closed orbit*. By design, this orbit usually travels through the center of each element. The relativistic Lorentz force is given by

$$\frac{d\mathbf{p}}{dt} = \frac{d(\gamma m \mathbf{v})}{dt} = e\left(\mathbf{E} + \mathbf{v} \times \mathbf{B}\right) \tag{2.1}$$

so that particles which have different energies will experience different deflections, and have different closed orbits. As long as the energy deviation is small, the new closed orbit will shift by an amount proportional to that deviation. We can then define the dispersion function $\eta(s)$ as the ratio of the closed orbit displacement at longitudinal position s to the fractional energy difference:

$$\eta(s) = \frac{\Delta x_{\mathrm{co}}(s)}{\Delta E / E_0}. \tag{2.2}$$

With that definition, we can write the transverse position of a particle as the sum of its dispersive orbit displacement and its betatron amplitude:

$$x = x_\beta + \eta\,\frac{\Delta E}{E_0}. \tag{2.3}$$

Now consider the case of a particle with energy E_0 that emits a photon of energy ϵ. Neither the particle's position nor its trajectory changes (although this statement will be revisited in the section on vertical emittance), but it does have a new energy and, therefore, a new off-energy closed orbit. To compensate for the change in closed orbit, the particle's betatron amplitude must change according to

$$
\begin{aligned}
\delta x = 0 = \delta x_\beta + \eta\,\frac{\epsilon}{E_0} &\quad\rightarrow\quad \delta x_\beta = -\eta\,\frac{\epsilon}{E_0} \\
\delta x' = 0 = \delta x'_\beta + \eta'\,\frac{\epsilon}{E_0} &\quad\rightarrow\quad \delta x'_\beta = -\eta'\,\frac{\epsilon}{E_0}.
\end{aligned}
\tag{2.4}
$$

where primed quantities are derivatives with respect to longitudinal position.

The particle's original motion in phase space was described by an invariant ellipse with area given by

$$\pi\left(a^2\right) = \pi\left(\gamma x^2 + 2\alpha x x' + \beta x'^2\right). \tag{2.5}$$

where α, β, and γ are the Twiss parameters and a is invariant as long as the motion is linear. After the emission of the photon, the ellipse has changed, and if the values from Eqs. 2.4 are inserted into Eq. 2.5, the resulting change in the area of the ellipse is

$$
\begin{aligned}
\delta a^2 &= \gamma\,\delta(x_\beta^2) + 2\alpha\,\delta(x_\beta x_\beta') + \beta\,\delta(x_\beta'^2) \\
&= \gamma\left[\left(x_{\beta 0} + \delta x_\beta\right)^2 - x_{\beta 0}^2\right] \\
&\quad + 2\alpha\left[\left(x_{\beta 0} + \delta x_\beta\right)\left(x_{\beta 0}' + \delta x_\beta'\right) - x_{\beta 0}x_{\beta 0}'\right] \\
&\quad + \beta\left[\left(x_{\beta 0}' + \delta x_\beta'\right)^2 - x_{\beta 0}'^2\right].
\end{aligned}
\tag{2.6}
$$

This expression depends upon the initial phase of the betatron motion, which enters through $x_{\beta 0}$ and $x_{\beta 0}'$. However, since all betatron phases are equally likely to emit a photon (to good approximation), we average over all phases. By doing this, any term that depends linearly on the initial phase vanishes, and we are left with

$$\left\langle \delta a^2 \right\rangle = \gamma(\delta x_\beta)^2 + 2\alpha(\delta x_\beta)(\delta x_\beta') + \beta(\delta x_\beta')^2. \tag{2.7}$$

Finally, inserting the values from Eqs. 2.4 gives

$$\left\langle \delta a^2 \right\rangle = \frac{\epsilon^2}{E_0^2}\left(\gamma \eta^2 + 2\alpha \eta \eta' + \beta \eta'^2\right) \tag{2.8}$$

which we can write more compactly by defining a function

$$\mathcal{H}(s) = \gamma \eta^2 + 2\alpha \eta \eta' + \beta \eta'^2 \tag{2.9}$$

14

where all terms on the right-hand-side are functions of the longitudinal position s.

This is the average change in amplitude due to the emission of a photon of a specific energy at a specific location in the ring. Now we would like to generalize this result to the average change due to all photons emitted at all ring locations. If the number of photons at energy ϵ emitted per unit time is given by $\dot{n}(\epsilon)$, then we get

$$\frac{d\langle a^2 \rangle}{dt} = \frac{1}{CE_0^2} \oint \left[\int \epsilon^2 \dot{n}(\epsilon)\, d\epsilon \right] \mathcal{H}(s)\, ds \tag{2.10}$$

where C is the circumference of the ring. The function $\dot{n}(\epsilon)$ depends on the local radius of curvature, and therefore, depends on the longitudinal position. The inner integral can be replaced by the total photon flux times the average of the square of the photon energy:

$$\int_0^\infty \epsilon^2 \dot{n}(\epsilon)\, d\epsilon = \dot{N} \left\langle \epsilon^2 \right\rangle. \tag{2.11}$$

Finally, averaging around the ring (denoted by the subscript s) gives

$$\frac{d\langle a^2 \rangle}{dt} = \frac{1}{E_0^2} \left\langle \dot{N} \left\langle \epsilon^2 \right\rangle \mathcal{H}(s) \right\rangle_s \tag{2.12}$$

This expression tells us the excitation due to radiation, which will drive the phase-space-volume of the beam larger until it is balanced by radiation damping.

The rate of change in the phase space ellipse due to damping is given by

$$\left. \frac{d\langle a^2 \rangle}{dt} \right|_{\text{damping}} = \frac{\langle P_\gamma \rangle}{E_0} \left\langle a^2 \right\rangle J_x \tag{2.13}$$

where J_x is the horizontal damping partition number, which is a constant for the ring, and P_γ is the radiated power, which also depends on the local radius of curvature:

$$P_\gamma = \frac{cC_\gamma}{2\pi} e^2 c \frac{E_0^4}{\rho^2} \tag{2.14}$$

15

where C_γ is a constant.

When excitation and damping are balanced, Eqs. 2.12 and 2.13 are equal. Then we have

$$\left\langle a^2 \right\rangle = \frac{1}{E_0} \frac{\left\langle \dot{N} \left\langle \epsilon^2 \right\rangle \mathcal{H} \right\rangle}{J_x \left\langle P_\gamma \right\rangle}. \tag{2.15}$$

With the photon flux given by

$$\dot{N}_{ph} \left\langle \epsilon^2 \right\rangle = \frac{55}{32\pi\sqrt{3}} \left[c\, C_\gamma \hbar c (mc^2)^4 \right] \gamma^7 \frac{1}{\rho^3}, \tag{2.16}$$

we can write Eq. 2.15 as a function of the local lattice functions and radius of curvature as

$$\left\langle a^2 \right\rangle = \frac{1}{J_x} \frac{\left\langle \mathcal{H}/\rho^3 \right\rangle}{\left\langle 1/\rho^2 \right\rangle} \frac{55}{16\sqrt{3}} \frac{\hbar c \gamma^2}{mc^2}. \tag{2.17}$$

At equilibrium, the particle's motion is sinusoidal, with amplitude given by $a\sqrt{\beta}$, so the mean square value is

$$\sigma^2 = \frac{1}{2} a^2 \beta \tag{2.18}$$

and we are left with the final expression for the horizontal emittance

$$\epsilon_x = \frac{\sigma^2}{\beta} = C_q\, \gamma^2 \frac{\left\langle \mathcal{H}/|\rho|^3 \right\rangle}{\mathcal{J}_x \left\langle 1/\rho^2 \right\rangle} \tag{2.19}$$

where

$$C_q = \frac{55}{32\sqrt{3}} \frac{\hbar c}{mc^2}. \tag{2.20}$$

2.2.2 Wiggler-Dominated Emittance

The twelve superconducting wigglers in CESR provide most of the synchrotron radiation radiation damping in the ring (approximately 90%). The ILC damping rings are also wiggler dominated, and in fact, the ability to study dynamics in the wiggler-dominated condition is a major motivation for the CesrTA project. As it concerns the calculation of emittance, two comments can be made.
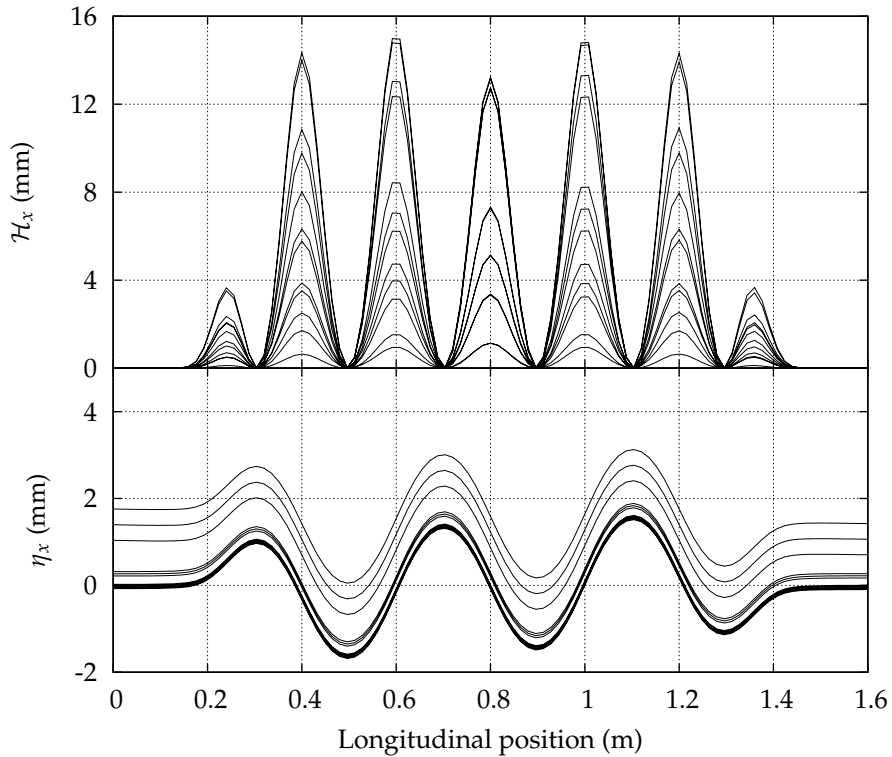
Figure 2.1: Wiggler radiation calculation. The top plot shows the $\mathcal{H}$ function inside each wiggler, and the bottom plot shows the internal dispersion. Variation in $\mathcal{H}$ between wigglers is due to different β-functions.

Internal Dispersion

When calculating the emittance in a ring (or many other parameters), it is common practice to average over the ring by taking values at the end of each element. This makes the reasonable assumption that β, η, etc., are changing slowly on the length scale of the typical element. Since the wigglers in CesrTA are located in (nearly) dispersion free regions, $\mathcal{H}$ is also zero, and this leads one to erroneously conclude that they contribute nothing to the overall excitation.

The wigglers dominate because of the fact that, while $\mathcal{H}$ is zero at the entrance and exit to each wiggler, it is nonzero *inside* the wigglers [13]. This can be

17

Table 2.1: Contribution to radiation integrals from wigglers and bends in CesrTA.

Integral	Bends	Wigglers
I_2 (m^{-2})	0.0959	0.871
I_{5a} (m^{-2})	1.55×10^{-4}	3.81×10^{-4}

seen in Fig. 2.1, which shows the η_x and $\mathcal{H}$ inside each wiggler. The spectrum of amplitudes for $\mathcal{H}$ is caused by different β-functions in different wigglers. As the next comment will show, including the internal dispersion is critical for the emittance calculation in CesrTA.

Optimal Number of Wigglers

Equation 2.19 is a ratio of averages, and those averages are often written as integrals around the ring:

$$\epsilon_x = C_q \gamma^2 \frac{I_5}{I_2} \qquad \text{where} \tag{2.21}$$

$$I_2 = \oint 1/\rho^2 \, ds \tag{2.22}$$

$$I_5 = \oint \mathcal{H}/|\rho|^3 \, ds. \tag{2.23}$$

Therefore, one can break up the emittance calculation into a part due to wigglers and a part due to bends (all other contributions are negligible). The relative contributions from each element type are shown in Table 2.1.

Using the separate values for the radiation integrals, it is possible to write a simple model for the emittance in CesrTA as a function of the number of wigglers. The emittance is given by

$$\epsilon_x = C_q \gamma^2 \frac{I_{5,\text{bend}} + n\, I_{5,\text{wiggler}}}{I_{2,\text{bend}} + n\, I_{2,\text{wiggler}}} \tag{2.24}$$

18
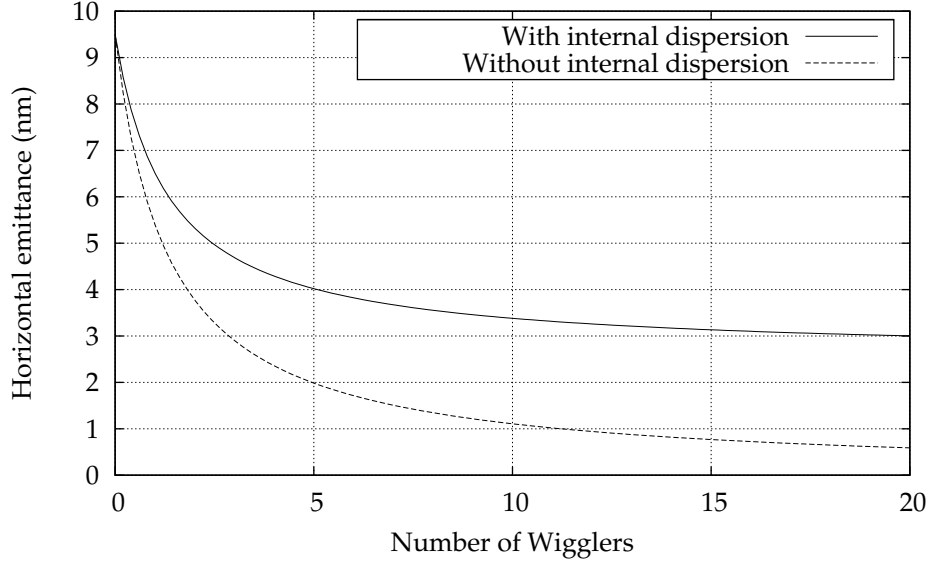
Figure 2.2: Wiggler radiation calculation. This shows the horizontal emittance in the CesrTA lattice as a function of the number of wigglers. It is evident that increasing the number of wigglers past the current number of 12 is not significant for reducing emittance. With 12 wigglers, the emittance is approximately three times as large with the correct calculation including internal dispersion.

where n is the number of wigglers and the wiggler terms are the average over the twelve wigglers in the current design.

If we ignore the internal dispersion in the wigglers, then n appears only in the denominator of Eq. 2.24, and the emittance approaches zero as n becomes very large. If the internal dispersion is included, then n appears in the numerator as well, and the emittance approaches

$$\epsilon_x \approx C_q \frac{\gamma^2}{\mathcal{J}_x} \frac{8\beta_x}{15\pi\, k_p^2\, \rho_w^3} \tag{2.25}$$

where k_p and ρ_w are the wave-number and bend radius of the wigglers. This different limiting behavior is shown in Fig. 2.2.

2.3 Vertical Emittance

Equation 2.19 was derived for the horizontal emittance, and it assumed that the horizontal lattice functions (the terms in $\mathcal{H}$) are well-known. Furthermore, it assumed that the horizontal dispersion was large enough that, when a particle emitted a photon, the dominant effect would be the change in the particle's energy and the consequences of that change due to dispersion.

Those assumptions are not valid for the vertical emittance, since most damping rings lie in the horizontal plane, and the vertical dispersion is much smaller (and usually assumed to be zero). We now turn to the problem of calculating the vertical emittance for a ring with no vertical dispersion and for a ring with finite vertical dispersion due to element misalignments.

2.3.1 Radiation Limit

If a particle with energy E_0 emits a photon of energy ϵ, the particle receives a kick due to the momentum carried off by that photon. We ignored this in the horizontal case, but we now look at it explicitly. The changes in the vertical coordinates are given by

$$\delta y = 0$$
$$\delta y' = \frac{\epsilon}{E_0}\theta_\gamma.$$

(2.26)

where θ_γ is the emission angle of the photon which is approximately equal to $1/\gamma$. From there, the derivation follows the same procedure as Eq. 2.19. That leads to a vertical emittance of

$$\epsilon_y = \frac{C_q}{2\,J_y}\frac{\langle \beta_y \rangle}{}\frac{\langle 1/\rho^3 \rangle}{\langle 1/\rho^2 \rangle}$$

(2.27)

which is smaller than the horizontal emittance by approximately a factor of $1/\gamma^2$.

2.3.2 Element Misalignments

The radiation limit just presented is only a lower limit. Element misalignments also increase vertical emittance by generating vertical dispersion and coupling. Here we will derive explicit formulas for that contribution, and in the next chapter, we will show that this effect, in general, overwhelms the radiation limit.

The dispersion in a damping ring is described by a differential equation that is similar to a driven harmonic oscillator, with the modification that the restoring and driving forces are periodic, rather than constant. That period is at least as small as the entire circumference of the ring, but may be smaller in rings with greater symmetry.

For a restoring force K_1 (given by the focusing strength), and a driving force F, the vertical dispersion obeys the following equation

$$\frac{d^2\eta_y}{ds^2} - K_1\eta_y = F. \tag{2.28}$$

where all parameters are functions of the longitudinal position s. The solution of Eq. 2.28 is given by

$$\eta_y(s) = \frac{\sqrt{\beta_y}}{2\sin \pi\nu_y} \oint \sqrt{\beta_y(s')} \cos\left(\psi_y(s) - \psi_y(s') + \pi\nu_y\right) F(s')\,ds'^{1}. \tag{2.29}$$

In the usual calculation of the horizontal dispersion, the driving term is dominated by the bending magnets. By design, most damping rings, including CesrTA, lie entirely in the horizontal plane. They have no vertical bending, and therefore, the principle contributions come from vertical offsets and rotations of the quadrupoles, and the vertical offsets of the sextupoles. In this case, the driving function in Eq. 2.28 becomes

$$F_y \simeq K_1 y_c - \widetilde{K}_1\eta_x + K_2 y_c\eta_x \tag{2.30}$$

---

[1]The above expression appears most often in the literature. However, in order to account for the phase discontinuity at the end of the ring, the cosine term should be written as $\cos\left(|\psi_y(s) - \psi_y(s')| - \pi\nu_y\right)$ [14]

where $\widetilde{K}_1$ and K_2 are the normalized skew quadrupole and sextupoles strengths, and y_c is the vertical closed orbit [15].

The first term in Eq. 2.30 gives the displacement of the vertical closed orbit relative to the center of a quadrupole, but if the closed orbit is assumed to be zero, it can also be interpreted as the vertical displacement of the quadrupole itself. The same argument applies to the last term and the vertical displacement of the sextupoles.

The second term is the contribution from a skew quadrupole, but it also describes normal quadrupoles which are rotated by arbitrary amounts. We can calculate the effect of all three misalignments in a similar fashion, but since the skew quad term is slightly more involved, we present it here as an example.

First consider the 4×4 transfer matrix of an upright quadrupole, and the matrix to rotate the four transverse coordinates $\mathbf{x}$ of a particle by an angle θ:

$$\mathbf{M_{quad}} \times \mathbf{x} = \begin{pmatrix} 1 & 0 & 0 & 0 \\ -\frac{1}{f} & 1 & 0 & 0 \\ 0 & 0 & 1 & 0 \\ 0 & 0 & \frac{1}{f} & 1 \end{pmatrix} \times \begin{pmatrix} x \\ x' \\ y \\ y' \end{pmatrix} \tag{2.31}$$

$$\mathbf{M_{rot}}(\theta) \times \mathbf{x} = \begin{pmatrix} \cos\theta & 0 & \sin\theta & 0 \\ 0 & \cos\theta & 0 & \sin\theta \\ -\sin\theta & 0 & \cos\theta & 0 \\ 0 & -\sin\theta & 0 & \cos\theta \end{pmatrix} \times \begin{pmatrix} x \\ x' \\ y \\ y' \end{pmatrix}. \tag{2.32}$$

$$\tag{2.33}$$

Rotating the quadrupole is equivalent to rotating the particle's coordinates (or dispersion parameters) by the same angle before the quad, then by the opposite angle after the quadrupole, so the transfer matrix of a rotated quadrupole

is

$$\widetilde{\mathbf{M}}_{\mathbf{quad}} = \mathbf{M}_{\mathbf{rot}}(-\theta) \cdot \mathbf{M}_{\mathbf{quad}} \cdot \mathbf{M}_{\mathbf{rot}}(\theta) \tag{2.34}$$

$$= \begin{pmatrix} 1 & 0 & 0 & 0 \\ -\dfrac{\cos(2\theta)}{f} & 1 & -\dfrac{2\cos(\theta)\sin(\theta)}{f} & 0 \\ 0 & 0 & 1 & 0 \\ -\dfrac{2\cos(\theta)\sin(\theta)}{f} & 0 & \dfrac{\cos(2\theta)}{f} & 1 \end{pmatrix}. \tag{2.35}$$

For small rotations ($\theta \ll 1$)

$$\widetilde{\mathbf{M}}_{\mathbf{quad}} \approx \begin{pmatrix} 1 & 0 & 0 & 0 \\ -\dfrac{1}{f} & 1 & -\dfrac{2\theta}{f} & 0 \\ 0 & 0 & 1 & 0 \\ -\dfrac{2\theta}{f} & 0 & \dfrac{1}{f} & 1 \end{pmatrix}. \tag{2.36}$$

The $(4,1)$ and $(4,3)$ components give the effect on the vertical motion. From the $(4,3)$ component, the rotated quadrupole looks like the regular, upright quadrupole, which couples the outgoing η_y' to the incoming η_y. This is expected, since the rotation is assumed to be very small. On the other hand, the $(4,1)$ component shows that the quadrupole also couples the outgoing η_y' to the incoming η_x. The effective difference in strength is given by the factor 2θ. In other words, the effect of an upright quadrupole of strength K_1, which has a small rotation θ, is mathematically identical to a skew quadrupole of strength $2\theta K_1$.

If we now include only the skew quadrupole term (of the form just derived) in $F(s)$ and use the fact that K_1 is either constant (for each quadrupole, or zero everywhere else, then the integral in Eq. 2.29 becomes a sum over only the quadrupoles:

$$\eta_y(s) = \frac{\sqrt{\beta_y}}{2\sin\pi\nu_y} \sum_i \sqrt{\beta_{y,i}} \cos\left(\psi_y(s) - \psi_{y,i} + \pi\nu_y\right)\left(2K_{1,i}\, l_i\, \theta_i\, \eta_{x,i}\right) \tag{2.37}$$

We don't know the rotations of the individual quadrupoles, so it is not possible to evaluate Eq. 2.37 directly. The best we can do is estimate the mean-squared value of the vertical dispersion based on an estimate of the mean-squared quadrupole rotation. Assuming the values in Eq. 2.37 are uncorrelated, many terms vanish upon averaging and we get the simple estimate

$$\left\langle \eta_y^2 \right\rangle = \frac{\langle \beta_y \rangle}{2 \sin^2 \pi \nu_y} \left(\sum_{\text{quads}} \beta_y (K_1 \, l \, \eta_x)^2 \right) \left\langle \theta^2 \right\rangle. \tag{2.38}$$

Using the other misalignments as driving terms, we can calculate formulas [16]:

$$\left\langle y_{\text{co}}^2 \right\rangle = \frac{\langle \beta_y \rangle}{8 \sin^2 \pi \nu_y} \left(\sum_{\text{quadrupoles}} \beta_y (K_1 \, l)^2 \right) \left\langle \Delta Y_{\text{quadrupole}}^2 \right\rangle \tag{2.39}$$

$$\left\langle \eta_y^2 \right\rangle = \frac{\langle \beta_y \rangle}{8 \sin^2 \pi \nu_y} \left(\sum_{\text{sextupoles}} \beta_y (K_2 \, l \, \eta_x)^2 \right) \left\langle \Delta Y_{\text{sextupole}}^2 \right\rangle. \tag{2.40}$$

Note that that Eq. 2.39 also gives the mean-square dispersion $\left\langle \eta_y^2 \right\rangle$ due to quadrupole offsets if we interpret $\left\langle \Delta Y_{\text{quadrupole}}^2 \right\rangle$ as the closed orbit distortion from those offsets. This means that

$$\frac{\left\langle \eta_y^2 \right\rangle}{\left\langle \Delta Y_{\text{quadrupole}}^2 \right\rangle} \sim \left(\frac{\left\langle y_{\text{co}}^2 \right\rangle}{\left\langle \Delta Y_{\text{quadrupole}}^2 \right\rangle} \right)^2. \tag{2.41}$$

For isomagnetic rings, where the bend radius is either zero or a constant, we can write Eq. 2.19 so that the vertical emittance depends upon the vertical dispersion according to

$$\epsilon_y = 2 J_\epsilon \frac{\left\langle \eta_y^2 \right\rangle}{\langle \beta_y \rangle} \left(\frac{\sigma_E}{E_0} \right)^2. \tag{2.42}$$

so we expect that the emittance depends quadratically on the misalignment amplitude. These formulas will be used to check the simulations presented in the next chapter.

Chapter 3
Impact of Magnet Misalignments in CesrTA

This chapter evaluates the effect of magnet misalignments on the vertical emittance in the CesrTA design. This is a characterization of the *uncorrected* emittance. Although we will, ultimately, be more interested in the *corrected* emittance, considering the uncorrected emittance is valuable for a few reasons:

1. The emittance and dispersion of the simulated, uncorrected damping ring can be compared more easily with theoretical calculations.

2. A potential strategy for achieving a minimum corrected emittance is to improve the initial alignment of the optics. In order to evaluate this option and develop an efficient strategy, a detailed understanding of which misalignments have the largest impact will be critical.

3. Some classes of misalignment (e.g., due to ground motion) may occur on a timescale too fast to be corrected. The fully characterized dependence of emittance on misalignments can be used to specify tolerances for these misalignments.

3.1   Misalignment Values

To predict the level of misalignment in CesrTA, we rely on survey data about the present state of CESR, and on predictions of what improvement may be achieved given the greater focus in CesrTA on low emittance. In the end, we present putative misalignments that are considered nominal for the purposes of
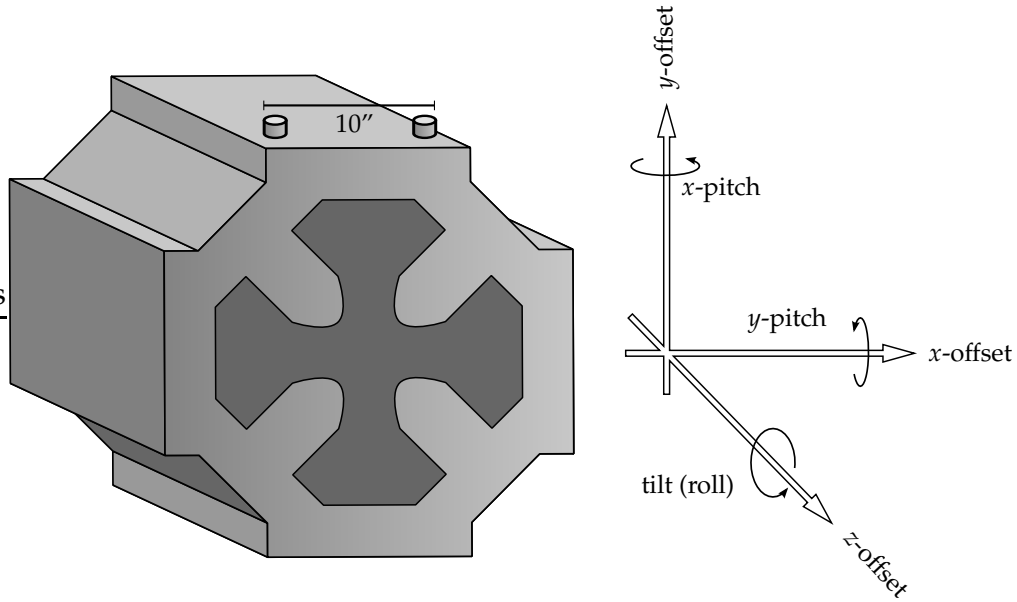
Figure 3.1: Diagram of misalignment parameters.

this study. Since the realistic misalignments may turn out to be worse (or better) than these estimates, we show a range of misalignment levels at each step.

3.1.1   Magnet Misalignment

Figure 3.1 shows the six possible misalignment parameters for each element. Of the six, only the horizontal and vertical offsets and the tilts have received much attention. Of those three, we will show that only the last two are of much concern, so we next look at the available data on the vertical offsets and tilts.

Figure 3.2 shows data accumulated for the quadrupoles during the years 2006-2007. We can observe that, with some outliers, the data has an approximately normal distribution with $\sigma = 70\,\mu m$ from the fit (the RMS of all data points is $100\,\mu m$) [17]. From here on, we will assume that all misalignments are normally distributed.
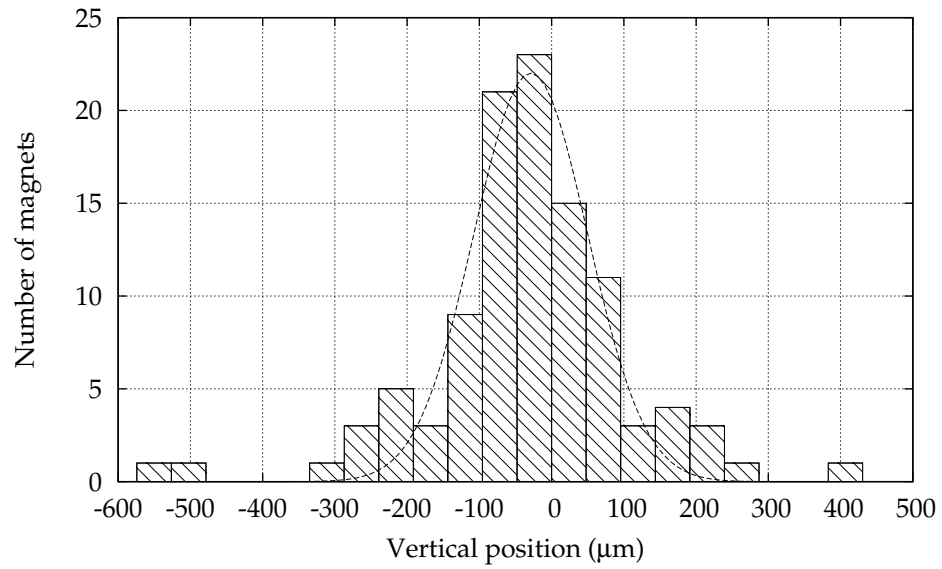
Figure 3.2: Vertical quadrupole survey. The RMS vertical offset for all quads in this sample is 100 μm.
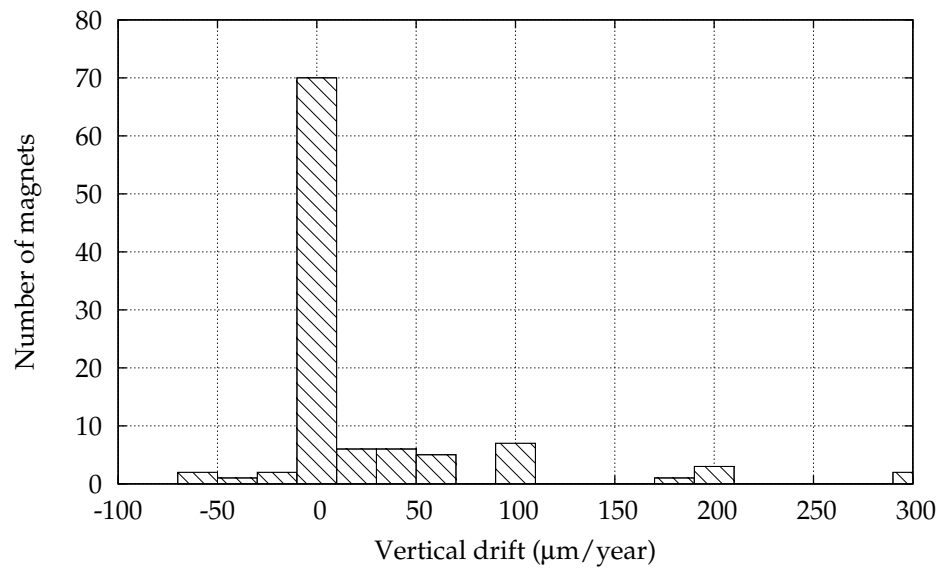
Figure 3.3: Long-term magnet motion. The yearly drift is a few tens of microns, which is around 10 μm for most magnets, which is smaller than our tolerance for uncorrected misalignments.

The magnets move continuously, so we need an estimate of how far their actual positions may have drifted since last surveyed. The yearly drift in the vertical magnet position is shown in Fig. 3.3 to be less than a few tens of microns per year for the vast majority of CESR magnets. Since this is much smaller than the variation in the surveyed position, we can trust that the surveyed variation is a reasonable estimate of the true variation on a timescale of at least a few years. Therefore, we assume that the RMS horizontal and vertical misalignment for quadrupoles is 150 μm.

Magnet tilt is measured using a spirit level that attaches to bushings on the top of each magnet [18] (see diagram). We find an RMS tilt of approximately 270 μrad. It is expected, however, that for CesrTA that value can be improved to approximately 100 μrad. In any case, improvement beyond 100 μrad is unlikely, since the bushings are separated by 10″ and the machining tolerances of the magnets are approximately $\frac{1}{1000}$″ $\left(\frac{1/1000''}{10''} = 100 \,\mu\text{rad} \right)$.

So far, we have focused on quadrupoles, and we will show that they are, by, far, the biggest concern. There are three other magnet types that are are also important: dipoles, sextupoles, and wigglers. We don't have such detailed data on the other types, but given that they are mounted, surveyed, and aligned in a similar fashion, it is reasonable to expect a similar level of misalignment from them.

Sextupoles do present a slight exception to this because they are attached to the quads and not independently adjustable. The displacement of the sextupole is the same as the attached quadrupole, but if the quad has some vertical pitch, then the sextupole will have an additional displacement due to its lever arm relative to the quad. We estimate the RMS sextupole displacement to be approximately twice that of the quadrupoles [19].
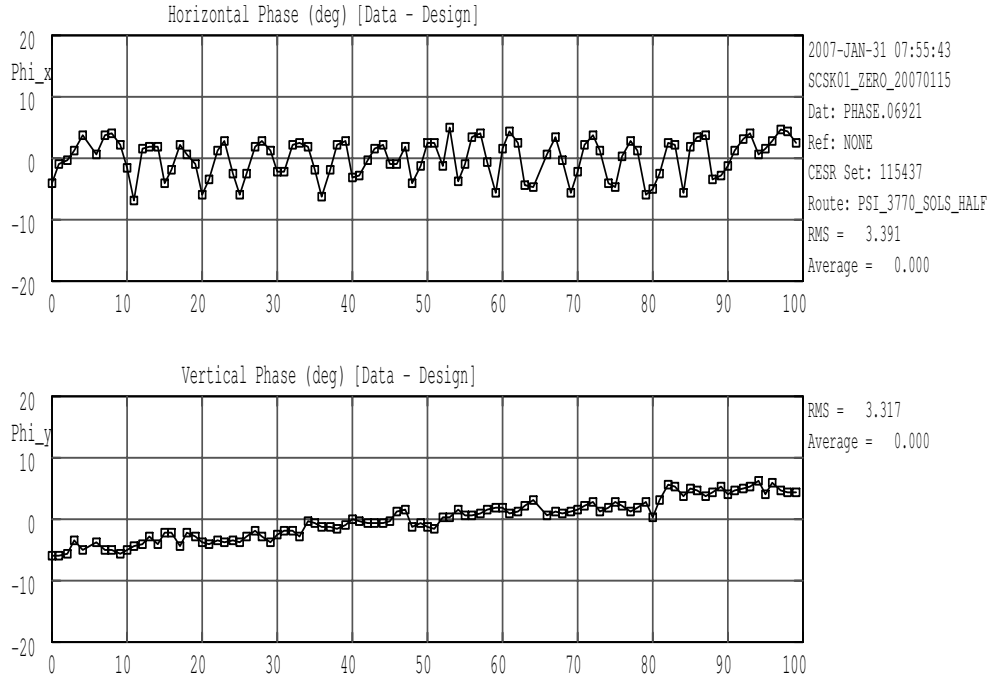
Figure 3.4: Phase residual in CESR after correction. This characterization data shows RMS ϕ_x=3.391° and ϕ_y=3.317° (59.2 and 57.9 mrad, respectively).

3.1.2 Quadrupole Field Strength

Due to calibration errors, power supplies, etc., the quadrupole field strengths deviate from the design values. This changes the betatron phase advance with respect to the design, which potentially impacts the emittance by changing the dispersion. More importantly, to the extent that the phase advance is not known, it becomes more difficult to model the effect of the corrector magnets that will be used in the next chapter.

In CESR, the phase is corrected by varying the quadrupole strengths until the measured phase matches the design. After correction, there is still some residual phase error, so here we try to estimate the corresponding quad strength error.
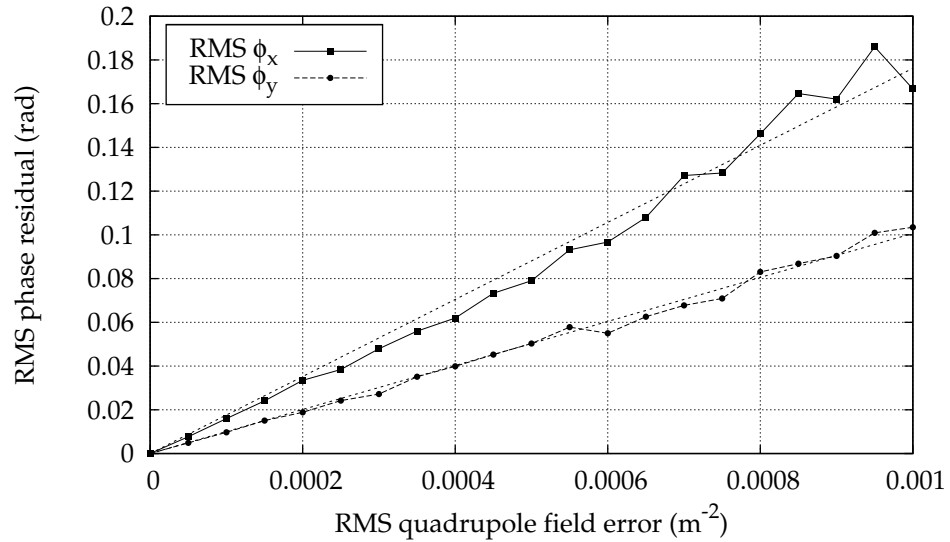
Figure 3.5: Simulated phase residual from quadrupole field errors. The RMS horizontal and vertical phase residuals are proportional to the RMS quadrupole strength errors with coefficients of 176 and $101\,\mathrm{rad}\cdot\mathrm{m}^2$, respectively. Averaging the horizontal and vertical gives a best guess of $0.0004\,\mathrm{m}^{-2}$ for the quadrupole strength deviation.

Figure 3.4 shows a typical phase correction from January 31, 2007 [20]. The RMS horizontal and vertical phase residuals are 59.2 and 57.9 μrad, respectively. We assume that these are a typical values.

Next, Fig. 3.5 shows the simulated RMS phase residual as a function of the RMS quad strength error. From the fits, we can calculate that that the quad strength error that best reproduces the phase residual is approximately $0.0004\,\mathrm{m}^{-2}$. It is worth emphasizing that this is *after* correction.

3.1.3   Nominal Values

Table 3.1 shows the nominal misalignment values for CesrTA. Those values are used for the remainder of this document. We have not explicitly mentioned

Table 3.1: Nominal misalignment parameters values for CesrTA.

Element	Parameter	Value	Element	Parameter	Value
Quadrupole	x-offset	150 μm	Sextupole	x-offset	300 μm
	y-offset	150 μm		y-offset	300 μm
	z-offset	150 μm		z-offset	300 μm
	x-pitch	100 μrad		x-pitch	100 μrad
	y-pitch	100 μrad		y-pitch	100 μrad
	Tilt	100 μrad		Tilt	100 μrad
Bend	x-offset	150 μm	Wiggler	x-offset	150 μm
	y-offset	150 μm		y-offset	150 μm
	z-offset	150 μm		z-offset	150 μm
	x-pitch	100 μrad		x-pitch	100 μrad
	y-pitch	100 μrad		y-pitch	100 μrad
	Tilt	100 μrad		Tilt	100 μrad

rotations about axes other than the beam axis, or longitudinal offsets. They are not consequential in terms of vertical emittance, but to the extent that they are used in these simulations, we assume that they have the same amplitude as the other offsets and rotations for each particular element.

3.2 Simulation

Using the nominal misalignment values, we can now simulate the impact these misalignments will have on vertical emittance in CesrTA. Then, using the formulas given in the previous chapter, we can verify that the simulation gives reasonable results.

3.2.1 Procedure

There is the question of whether the normal distribution of misalignments should have a cutoff at very large amplitudes. A point in favor of the cutoff is that, for very large amplitudes, the ring can become unstable and the relevant parameters cannot be calculated. In the unlikely event that this happened in the physical ring, some other measures would need to be taken before one proceeded to store beam and tune the ring.

Other than mathematical convenience, there is little reason to trust that the extreme tails of the normal distribution correspond to reality anyway. Therefore, we impose a cutoff that no error be larger than than $\pm 3\sigma$.

From here, the procedure is simple. Normally-distributed random alignment errors are generated using the Numerical Recipes libraries [21]. The closed orbit, dispersion, and emittance are calculated for the misaligned ring, and the procedure is repeated until a sufficient statistical sample has been accumulated.

3.2.2 Comparison With Theory

Figure 3.6 shows the simulation of vertical offsets in quadrupoles and sextupoles. In both cases, we show a linear fit to the RMS vertical dispersion, and a quadratic fit to the emittance. For the quads, we also show a linear fit to the RMS vertical closed orbit. Other elements and misalignments are treated in the same way.

For each of the misalignments, we expect a linear relationship between the mean-square vertical dispersion and emittance according to Eq. 2.42. That relationship is verified in Fig. 3.7 which includes the dispersion and emittance data from every simulated misalignment parameter.
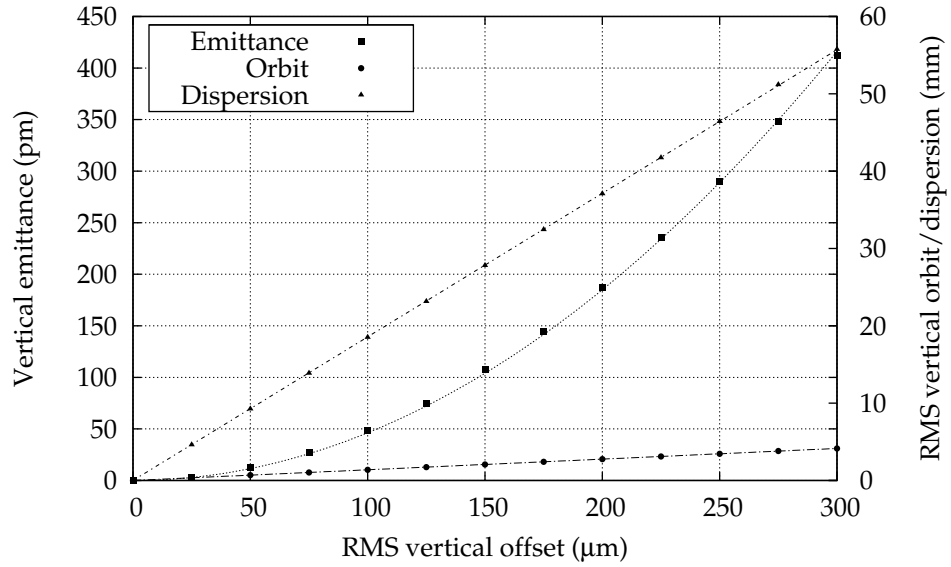
(a) Vertical quadrupole offset
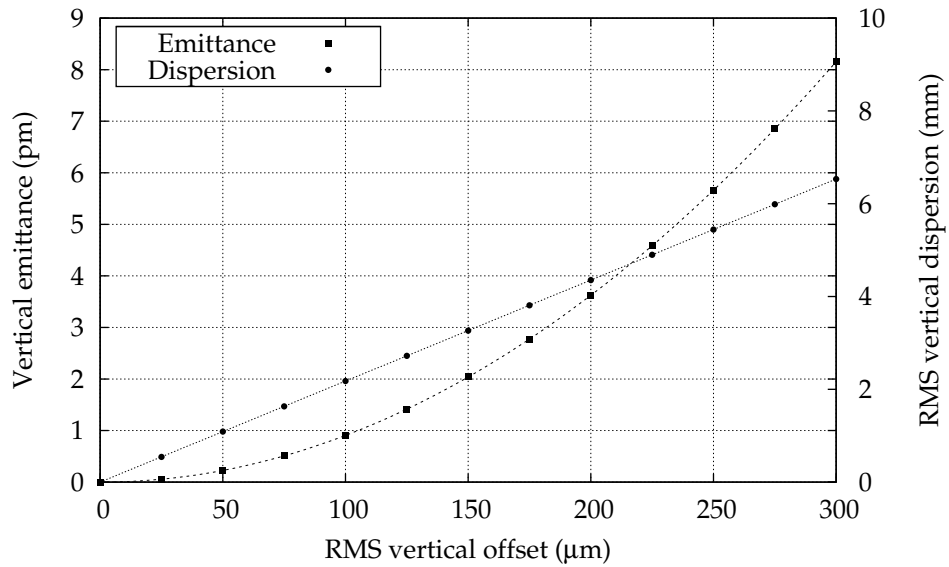
(b) Vertical sextupole offset

Figure 3.6: Simulated misalignment of quadrupoles and sextupoles. Linear fits are shown for dispersion and orbit (quadrupole only), and quadratic fits for emittance. The coefficients from the fits are in Table 3.4.
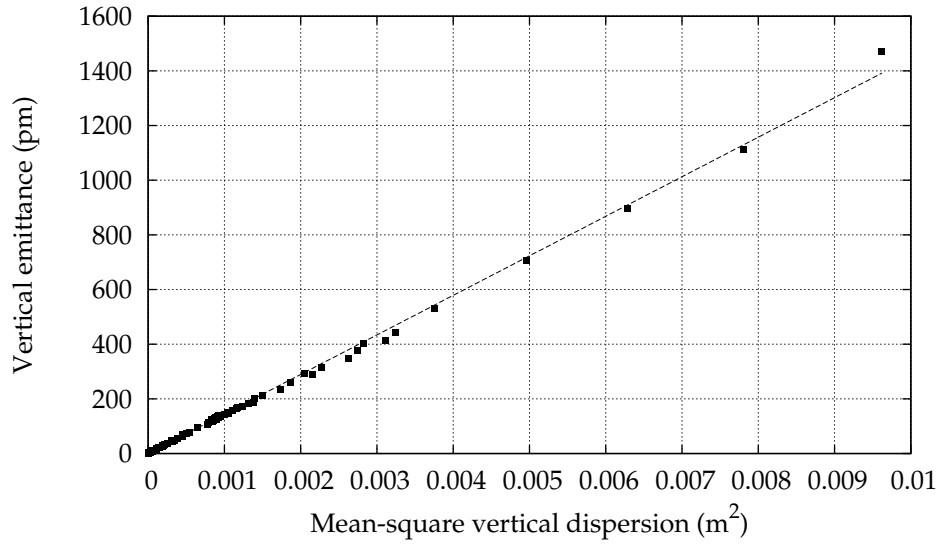
Figure 3.7: Emittance vs. vertical dispersion. This fit verifies the linear relationship used to calculate tolerances for uncorrected emittance.

The parameters from the fits in Figs. 3.6-3.7, as well as other relevant fits that are not shown, can be compared directly with the values predicted by Eqs. 2.38-2.40. This comparison, which shows very good agreement, is shown in Table 3.2.

3.2.3 Emittance Results

The results from the misalignment simulation from Table 3.3 show that only the five misalignment types contribute to the emittance at the picometer level or greater.

Since the emittance depends quadratically on the RMS dispersion, and the RMS dispersion is proportional to the RMS misalignment, it is possible to write down a simple model for the uncorrected emittance for arbitrary misalignments

$$\langle \epsilon_y \rangle = k \left\langle \Delta^2 \right\rangle \tag{3.1}$$

Table 3.2: Comparison of analytical and simulated misalignment quantities.

Quantity	Analytic	Simulation	Units
$\dfrac{\epsilon_y}{\left\langle \eta_y^2 \right\rangle}$	1.31	1.45	$\mathrm{m}^{-1}\left(\times 10^{-7}\right)$
$\sqrt{\dfrac{\left\langle y_{\mathrm{co}}^2 \right\rangle}{\left\langle \Delta Y_{\mathrm{quad}}^2 \right\rangle}}$	14.7	13.8	
$\sqrt{\dfrac{\left\langle \eta_y^2 \right\rangle}{\left\langle \Delta Y_{\mathrm{quad}}^2 \right\rangle}}$	216	186	
$\sqrt{\dfrac{\left\langle \eta_y^2 \right\rangle}{\left\langle \Delta \Theta_{\mathrm{quad}}^2 \right\rangle}}$	23.6	21.9	m
$\sqrt{\dfrac{\left\langle \eta_y^2 \right\rangle}{\left\langle \Delta Y_{\mathrm{sext}}^2 \right\rangle}}$	23.4	21.8	
$\sqrt{\dfrac{\left\langle y_{\mathrm{co}}^2 \right\rangle}{\left\langle \Delta Y_{\mathrm{wig}}^2 \right\rangle}}$	1.57	1.52	

where Δ is the amplitude of the misalignment parameter (either offset or rotation) and k is a constant for each particular misalignment parameter. The coefficient will depend on what confidence limit we chose for the dependent variable. We typically choose the median (50% level), but it is also possible to set a higher confidence, e.g., 95%, and get a different constant for the emittance corresponding to that limit.

Since the dispersion and orbit depend linearly on the misalignment amplitude, we can compute linear coefficients from the same data. The various values of k, found by the appropriate quadratic or linear fits to simulated data, are shown in Table 3.4. To the extent that the quadratic model is correct, one can generate the values in Table 3.3 from the values in Table 3.4, or vice versa.

3.3   Other Misalignment Tolerance Estimates

3.3.1   Ground Motion

Using the emittance coefficients in Table 3.4, and inverting Eq. 3.1, we can calculate the misalignment tolerances for any specified emittance. This is useful in cases where the misalignment cannot be corrected. For example, if we set an emittance threshold of 2 pm, then the approximate magnet alignment tolerances that correspond to that emittance are given in Table 3.5.

In Fig. 3.8, the vibration spectrum is shown for quad Q23W [22]. This motion happens too quickly to be corrected, but the data in the figure establishes that, for frequencies greater than 3 Hz, the RMS vertical motion is less than 1 μm. This is compatible, therefore with the 2 pm alignment tolerances established in Table 3.5.

Table 3.3: Vertical emittance and other measurements resulting from nominal misalignments.

Element	Parameter	ϵ_y (pm)		η_y (mm)	y (mm)	$\overline{C}_{12}$
		P_{50}	P_{95}			
Quadrupole	y-offset	101	262	26.4	1.96	5.04×10^{-2}
Sextupole	y-offset	7.29	17.9	6.33	9.53×10^{-5}	1.55×10^{-2}
Bend	tilt	6.22	16.9	6.71	5.08×10^{-1}	1.30×10^{-2}
Wiggler	y-offset	1.09	3.97	2.71	2.20×10^{-1}	5.09×10^{-3}
Quadrupole	tilt	8.60×10^{-1}	2.11	2.03	3.56×10^{-5}	6.00×10^{-3}
Wiggler	y-pitch	3.59×10^{-2}	1.18×10^{-1}	5.44×10^{-1}	2.53×10^{-3}	5.94×10^{-5}
Bend	y-pitch	1.02×10^{-3}	3.00×10^{-3}	8.05×10^{-2}	3.64×10^{-3}	1.76×10^{-4}
Bend	y-offset	4.96×10^{-4}	1.28×10^{-3}	5.74×10^{-2}	4.37×10^{-3}	1.13×10^{-4}
Wiggler	tilt	3.89×10^{-4}	1.59×10^{-3}	8.49×10^{-5}	1.37×10^{-6}	3.31×10^{-4}
Quadrupole	y-pitch	3.30×10^{-4}	1.04×10^{-3}	4.78×10^{-2}	3.58×10^{-3}	8.91×10^{-5}
Sextupole	y-pitch	4.60×10^{-6}	1.12×10^{-5}	4.59×10^{-3}	1.02×10^{-7}	1.75×10^{-5}
Sextupole	tilt	1.70×10^{-9}	4.77×10^{-9}	9.62×10^{-5}	1.39×10^{-9}	2.38×10^{-7}

Table 3.4: Coefficients from misalignment fits. The emittance columns show the constants from the quadratic fit between the misalignment parameter and the vertical emittance (at two different confidence levels). The remaining two columns show the constant from a linear fit to the median dispersion and orbit.

| | | Quadratic constant (m^{-1}) | | Linear constant | |
| | | ϵ_y | | | |
Element	Parameter	P_{50}	P_{95}	η_y	y
quad	y-offset	4.28×10^{-3}	1.18×10^{-2}	174	131
bend	tilt	6.05×10^{-4}	1.62×10^{-3}	65.6	5.03
quad	tilt	8.57×10^{-5}	2.09×10^{-4}	20.7	3.58×10^{-4}
sext	y-offset	7.91×10^{-5}	1.94×10^{-4}	20.9	3.16×10^{-4}
wig	y-offset	4.86×10^{-5}	1.75×10^{-4}	18.1	1.46
wig	y-pitch	3.47×10^{-6}	1.22×10^{-5}	5.38	2.50×10^{-2}
bend	y-pitch	1.09×10^{-7}	2.94×10^{-7}	8.14×10^{-1}	3.66×10^{-2}
wig	tilt	4.13×10^{-8}	1.65×10^{-7}	8.02×10^{-4}	1.38×10^{-5}
quad	y-pitch	3.33×10^{-8}	1.04×10^{-7}	4.77×10^{-1}	3.66×10^{-2}
bend	y-offset	2.24×10^{-8}	5.79×10^{-8}	3.89×10^{-1}	2.91×10^{-2}
sext	y-pitch	4.66×10^{-10}	1.09×10^{-9}	4.65×10^{-2}	1.03×10^{-6}
sext	tilt	1.71×10^{-13}	4.45×10^{-13}	9.73×10^{-4}	1.33×10^{-8}

Table 3.5: Alignment tolerances for uncorrected emittance.

| | | ϵ_y=2 pm | | ϵ_y=10 pm | |
Element	Parameter	P_{50}	P_{95}	P_{50}	P_{95}
quad	y-offset (µm)	21.6	13.0	48.3	29.1
bend	tilt (µrad)	57.5	35.1	129	78.5
quad	tilt (µrad)	153	97.8	342	219
sext	y-offset (µm)	159	101	356	227
wig	y-offset (µm)	203	107	454	239
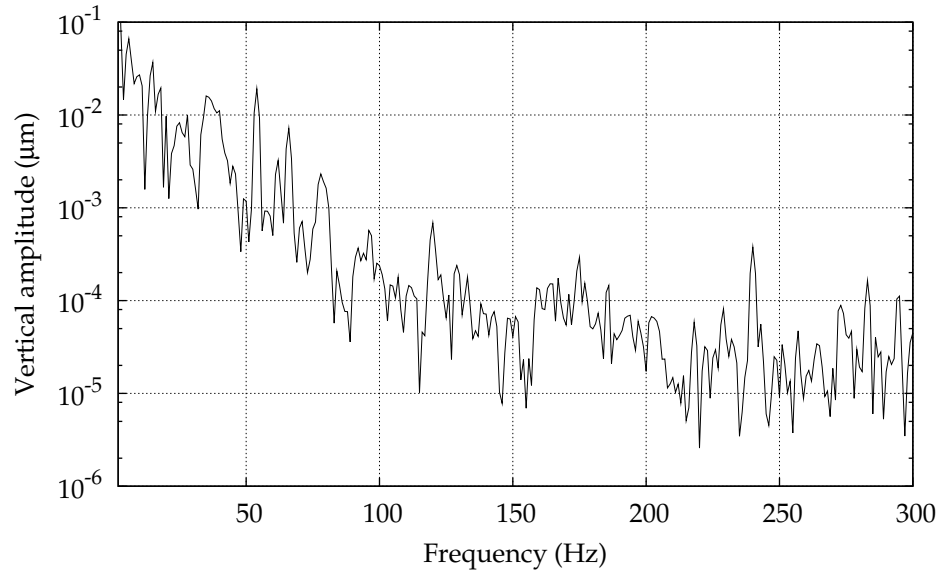
Figure 3.8: Ground motion at Q23. Above a few Hertz, the amplitude of ground motion is smaller than the tolerance for uncorrected emittance.

3.3.2 Slow-Wave Misalignments

So far, we have only considered uncorrelated misalignments. There are at least a couple of scenarios in CESR that merit looking at correlated, or *slow wave* misalignments. One potential source of slow-wave misalignment is the survey procedure itself, which surveys each magnet, in part, relative to its neighbors. Because of this, small errors can accumulate around the ring producing correlated misalignments that may be larger than our random estimates.

Another potential source of slow-wave misalignment is the temperature gradient in the accelerator tunnel, which causes different amounts of thermal expansion in different locations.

We model the slow-wave by introducing a sinusoidal misalignment with amplitude A that must close on itself at the end of the ring. This applies to
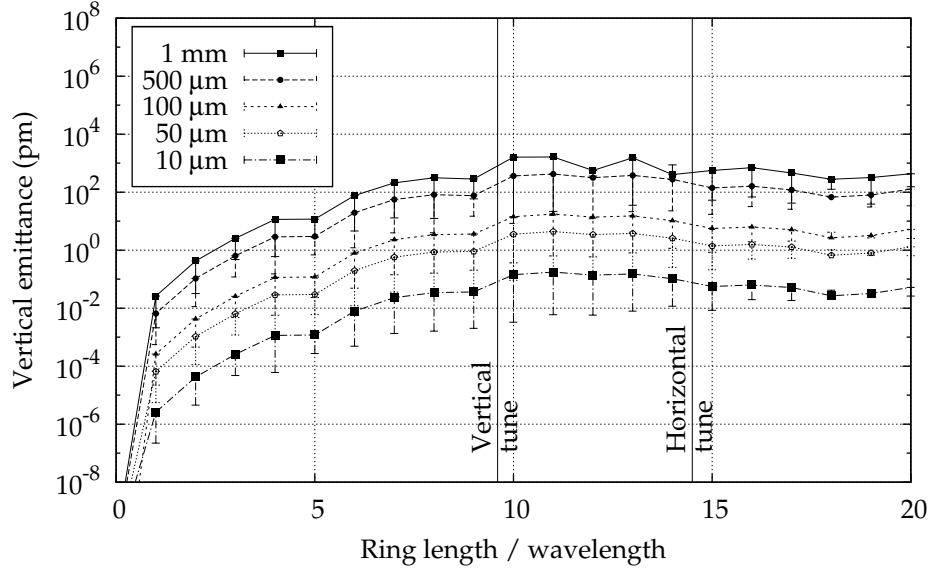
Figure 3.9: Simulation of slow-wave misalignment. Each curve corresponds to a different wave amplitude, and each point is an average over all phases of the wave.

every element, so the vertical offset at any point s in the ring is given by

$$\Delta y = A \sin (ks - \phi) \tag{3.2}$$

$$\text{with} \qquad k = \frac{2n\pi}{\text{ring length}}. \tag{3.3}$$

The phase ϕ adjusts where the slow wave has its extrema.

The slow-wave simulation is shown in Fig. 3.9 for various amplitudes. Each point represents the average and standard deviation over 100 values of ϕ between 0 and 2π. The effect on vertical emittance increases as the frequency of the wave approaches the vertical tune. However, typical thermal expansion is estimated to be about 30 μm [23]. Since it has a relatively slow wave that oscillates only a few times around the tunnel, the uncorrected emittance is well below our targets. For larger amplitudes or shorter wavelengths, the uncorrected emittance may not be satisfactory, and correction algorithms will be required.

Chapter 4
Optics Correction

In this chapter, we present an algorithm for minimizing the vertical emittance generated by magnet misalignments. The performance of the algorithm is simulated in a variety of possible scenarios for misalignment level and BPM resolution. The general algorithm can be run in a variety of configurations, but we focus on two simple configurations that are shown to be effective for CesrTA.

4.1   Correction Algorithm

The correction algorithm minimizes the vertical emittance by reducing the sources of emittance, specifically, vertical closed orbit and dispersion, and betatron coupling. We do this by varying the strength of corrector elements, such as steerings and skew quads.

For the uninitiated, it is a puzzling fact that the algorithm never considers the emittance directly. To understand this, consider the fact that when minimizing a function, one needs a way to determine how the function responds to a change in one of its parameters. For minimizing emittance, we could do this by changing a corrector in the physical ring and measuring the new emittance. However, there are many correctors, and measuring the response to each of them would ultimately require many hundreds, even thousands, of corrector changes and emittance measurements. This is impractical, or at best, extremely time consuming. Also it is difficult to measure the emittance with any precision.

Alternatively, we could use a model of the ring and simulate the response of the emittance to changes in the parameters. Unfortunately, since we don't

know the details of the misalignments in the physical ring, the model can't tell us what happens to the real emittance. In other words, since we don't know the misalignments, we *can't* model this aspect of the physical ring. If we did know the details of the actual misalignments, they would already be accounted for in the design of the ring, and correction of this sort would be irrelevant (or at least significantly less important). Since the model has no misalignments, it is already optimally tuned for low emittance, and a change to any corrector is likely to make the simulated emittance much worse.

Just as the unknown misalignments make it impossible for our model to predict the emittance in the physical ring, they also make it impossible for our model to predict the orbit, dispersion, and coupling in the physical ring. However, the model can be used to predict *changes* in those quantities, and that fact is what allows us to use the model ring in our algorithm. Furthermore, since we can measure those quantities fairly easily, we know how much they need to change.

Therefore, the job of the correction algorithm is to predict the corrector settings that will reduce the sources of emittance (orbit, dispersion, and coupling) from their measured values to their design values (usually zero). Since our model starts out with the design values, we actually proceed by solving the inverse problem: finding the corrector settings that will make the model look as bad as a measurement of the physical ring. As long as we make small enough changes to keep things fairly linear, then putting the opposite (negative) corrector settings into the physical rings will cause the opposite changes in the measured quantities, canceling the effect of the misalignments.

We can express this mathematically as follows: we have a set of measured quantities M and the same quantities calculated from the model m. The model

and the physical ring both have parameters P, so we want to find the values for P that minimize the following expression:

$$\chi^2 = \sum_i w_{M_i} \left(M_i - m_i\right)^2 \quad + \quad \sum_j w_{P_j} \left(\delta P_j\right)^2. \tag{4.1}$$

The first sum is simply the square of the residuals between the measured and calculated quantities. The second term provides an additional constraint on the changes to the parameters. This is helpful for two reasons. First, it tends to keep the iterative optimization process from wandering off into unstable regions. Second, in the physical ring, one expects better (i.e., more linear) behavior by making small adjustments to many elements, rather than large adjustments to a few elements.

Each term in each sum is weighted according to the values of w_{M_i} (for the measurements) and w_{P_j} (for the parameter changes). These could be different for each term, but in practice, the parameter weights and the measurement weights are usually uniform for each measurement type (e.g., orbit, dispersion, or coupling). A reasonable extension of this might be to weight the measurements at different detectors according to the lattice design, but we do not explore that here.

Once we have the values of P that minimize Eq. 4.1, the parameters in the physical ring are changed by $-P$, and if desired, the process is repeated with different parameters or measurements.

4.2   Simulation of the Algorithm

Simulating the correction algorithm is slightly more complicated than the procedure just described, since we must model the physical ring as well as the *model ring* used for the minimization. Figure 4.1 shows the relationship between the
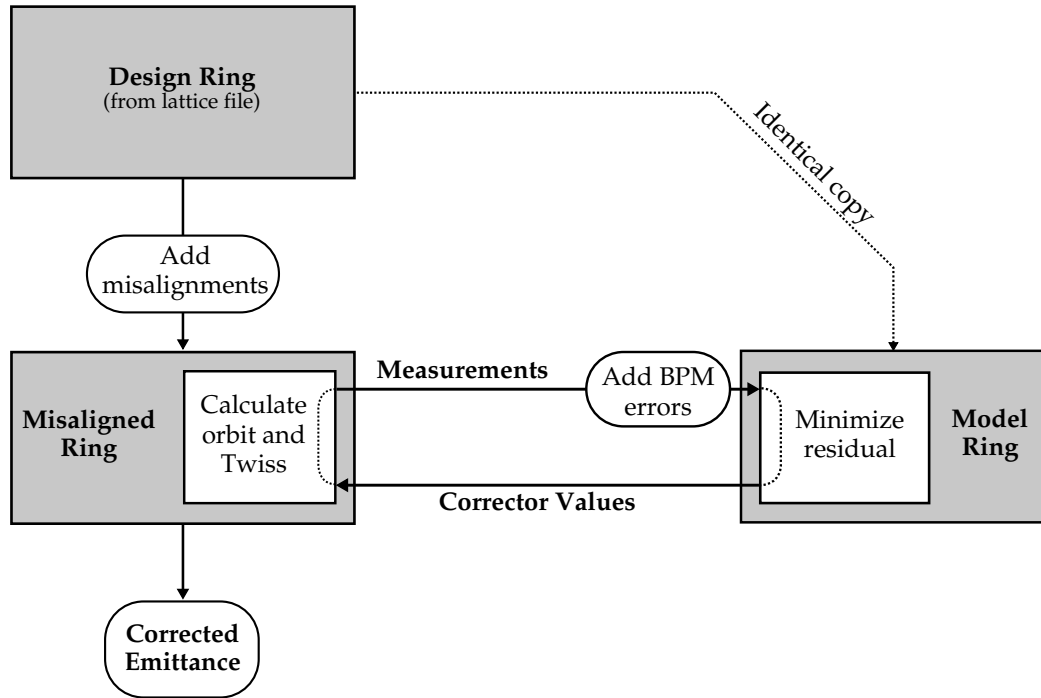
Figure 4.1: Schematic of correction algorithm.

various models. We start with the *design ring* which comes directly from the lattice file–it has no misalignments, and therefore, negligible vertical emittance. A copy of that ring is made and the copy's elements are given random misalignments; therefore, it is called the *misaligned ring*. The *misaligned ring* has nonzero vertical emittance, and represents the physical ring.

A second copy of of the design ring is made, called the *model ring*, which is used to model how parameter changes will affect the *misaligned ring* (as discussed in the previous section). It is worth restating that the details of the physical misalignments are unknown, so they cannot be used anywhere in the minimization. Therefore, only measurable quantities can be extracted from the *misaligned ring*.

To make the simulation more realistic, when measurement quantities are passed from the *misaligned ring* to the minimizer for comparison with the *model*

ring, random errors are added to reproduce the effect of BPM errors. Once the minimizer is finished, the parameter values (or rather, their opposites) are loaded into the *misaligned ring* and the emittance can be calculated. Often, this process is repeated, taking new measurements and loading new corrections.

4.3   Beam Position Monitor Accuracy

The measurement values coming from the physical ring will contain errors caused by the physical or electronic properties of the BPMs. For example, BPMs may be misaligned or rotated, the internal button locations may be slightly different, or their may be slightly different gains from the different buttons. A reasonable way to model all of these effects is to introduce three types of BPM errors as follows:

Absolute resolution Uncertainty in the horizontal and vertical location of the beam after a single turn. This applies only to orbit measurements.

Differential resolution Uncertainty in the horizontal and vertical *difference* between two orbit measurements. This applies only to dispersion measurements, and because many systematic effects are subtracted out, is significantly smaller in magnitude than the absolute resolution.

Rotation resolution Degree to which the horizontal and vertical beam behavior gets mixed by the BPM. This effects orbit, dispersion, and coupling measurements (although the effect on coupling measurements is shown later to be very small).

4.3.1 Orbit and Dispersion with BPM errors

Applying BPM errors to the orbit measurement is straightforward. Random numbers of the appropriate magnitude are simply added to the measured horizontal and vertical measurement values. For the dispersion measurement, we first convert the differential resolution to a dispersion resolution by dividing by the energy change δ that is assumed to be used in the dispersion measurement. For these studies, we assume $\delta = 10^{-3}$. After applying the appropriate offsets, the horizontal and vertical values are rotated using the usual rotation matrix, by an angle given by the rotation resolution.

4.3.2 Coupling

The coupling in CESR is characterized by the $\overline{\mathbf{C}}$ matrix which relates the motion of the beam's normal-modes (A and B) to the motion seen in the laboratory frame (x and y) [24]. When the beam is driven to oscillate horizontally or vertically, measurement of the resulting motion in both planes is used to determine the appropriate matrix elements.

The coupling measurement is insensitive to the detector's location, but detector rotation is more complicated than in the orbit or dispersion measurements because the coupling involves both the horizontal and vertical beam motion simultaneously. The strategy so far has been to add errors to the measurements using only the measurements themselves and the amplitude of the errors. To do the same with coupling, we first need to work backward from $\overline{\mathbf{C}}$ to get the beam motion, then add the errors, and finally propagate those forward into the new coupling matrix.

When the beam is driven in the horizontal plane, two elements of the $\overline{\mathbf{C}}$ matrix are given by

$$\overline{C}_{12} = \gamma \sqrt{\frac{\beta_A}{\beta_B}} \left(\frac{y}{x}\right)_A \sin \Delta\phi_A \tag{4.2}$$

$$\overline{C}_{22} = \gamma \sqrt{\frac{\beta_A}{\beta_B}} \left(\frac{y}{x}\right)_A \cos \Delta\phi_A \tag{4.3}$$

where $\left(\frac{y}{x}\right)_A$ is the ratio of the amplitude of the vertical and horizontal motion and $\Delta\phi_A$ is the phase difference between the vertical and horizontal motion. The subscript A denotes the fact that driving in the horizontal plane excites primarily the A-like mode.

Once $\overline{\mathbf{C}}$ has been calculated from the (simulated) misaligned ring, we can invert Eqs. 4.2-4.3, describing the beam motion in terms of $\overline{\mathbf{C}}$ matrix elements as

$$\left(\frac{y}{x}\right)_A = \frac{1}{\gamma} \sqrt{\frac{\beta_B}{\beta_A}} \sqrt{\overline{C}_{12}^2 + \overline{C}_{22}^2} \tag{4.4}$$

$$\Delta\phi_A = \arctan\left(\overline{C}_{12}, \overline{C}_{22}\right) \tag{4.5}$$

where the values of β_A, β_B, and γ come from the lattice.[1]

Since we only care about the relative amplitude and phase of the horizontal and vertical motion, we can write the turn-by-turn position of the beam as

$$\begin{pmatrix} x \\ y \end{pmatrix}_{\text{rel}} = \begin{pmatrix} \cos(\omega t) \\ A\cos(\omega t - \phi). \end{pmatrix} \tag{4.6}$$

where the values of A and ϕ are given by Eqs. 4.4-4.5, and ω is the driving frequency.

---

[1]We use $\arctan(y, x) = \arctan\left(\frac{y}{x}\right)$, following the convention from Fortran and C. *Mathematica* reverses the order of the arguments.

If we now rotate the coordinates of that beam, which is equivalent to rotating the detector, we have

$$
\begin{pmatrix} x' \\ y' \end{pmatrix} = \begin{pmatrix} \cos\theta & \sin\theta \\ -\sin\theta & \cos\theta \end{pmatrix} \times \begin{pmatrix} \cos(\omega t) \\ A\cos(\omega t - \phi). \end{pmatrix}
$$

$$
= \begin{pmatrix} (A\cos\phi\sin\theta + \cos\theta)\cos\omega t + (A\sin\theta\sin\phi)\sin\omega t \\ (A\cos\phi\cos\theta - \sin\theta)\cos\omega t + (A\cos\theta\sin\phi)\sin\omega t \end{pmatrix}
$$

$$
= \underbrace{\begin{pmatrix} A\cos\phi\sin\theta + \cos\theta & A\sin\theta\sin\phi \\ A\cos\phi\cos\theta - \sin\theta & A\cos\theta\sin\phi \end{pmatrix}}_{\mathbf{M}} \times \begin{pmatrix} \cos\omega t \\ \sin\omega t \end{pmatrix} \tag{4.7}
$$

where the matrix $\mathbf{M}$ is defined as shown. Using the trigonometric identity

$$
a\cos x + b\sin x = \sqrt{a^2 + b^2}\,\cos\left(x - \arctan(b,\,a)\right) \tag{4.8}
$$

and the definitions

$$
A'_x = \sqrt{M_{11}^2 + M_{12}^2} \qquad\qquad \phi'_x = \arctan(M_{12},\,M_{11}) \tag{4.9}
$$
$$
A'_y = \sqrt{M_{21}^2 + M_{22}^2} \qquad\qquad \phi'_y = \arctan(M_{22},\,M_{21})
$$

the motion of the beam in a rotated detector is given by

$$
\begin{pmatrix} x' \\ y' \end{pmatrix} = \begin{pmatrix} A'_x\cos(\omega t - \phi'_x) \\ A'_y\cos(\omega t - \phi'_y) \end{pmatrix}. \tag{4.10}
$$

As before, we only care about the relative motion, so the equation can be rewritten

$$
\begin{pmatrix} x' \\ y' \end{pmatrix}_{\text{rel}} = \begin{pmatrix} \cos(\omega t) \\ A'\cos(\omega t - \Delta\phi') \end{pmatrix} \tag{4.11}
$$

where $A' \equiv A'_y/A'_x$ and $\Delta\phi' \equiv (\phi'_y - \phi'_x)$.

Finally, according to the definitions of of the $\overline{\mathbf{C}}$ matrix elements given in Eqs. 4.2-4.3, the apparent $\overline{\mathbf{C}}$ elements from a rotated detector are given by

$$\overline{C}'_{12} = \gamma \sqrt{\frac{\beta_A}{\beta_B}} A' \sin \Delta\phi' \tag{4.12}$$

$$\overline{C}'_{22} = \gamma \sqrt{\frac{\beta_A}{\beta_B}} A' \cos \Delta\phi' \tag{4.13}$$

The lattice functions in the final result are independent of BPM rotations because they are calculated from the lattice, not measured.

When the rotation angles of the BPMs are small, these rather cumbersome expressions reduce to

$$\overline{C}'_{12} \approx \overline{C}_{12} \left(1 - 2\theta\, \overline{C}_{22}\right) \tag{4.14}$$

$$\overline{C}'_{22} \approx \overline{C}_{22} + \theta \left(\overline{C}^2_{12} - \overline{C}^2_{22} - 1\right). \tag{4.15}$$

We are primarily interested in $\overline{C}_{12}$, but there are two interesting features of this result. First, in the absence of any genuine coupling at a given detector, even a rotated detector will report zero coupling. This is different from the orbit and dispersion measurements where detector rotations *create* false signals, and it comes from the measurement technique, where the use of the phase information prevents the signal from the horizontal motion from *leaking* into the vertical.

Second, in the limit of small coupling where $\overline{C}_{12}, \overline{C}_{22} \ll 1$, the measured $\overline{C}_{22}$ is equal to the detector rotation. Knowing the detector rotation would allow us to remove that error from the orbit and dispersion measurements.

4.3.3   Limits from Detector Resolution

The resolution of the detectors sets a limit on how well the various optical parameters can be corrected. For example, in the unreasonable case that a ring had no vertical dispersion, detector resolution would cause the measured values to

Table 4.1: Correction limits from BPM resolution. These coefficients deter-
mine the level of errors created by BPMs in a perfectly aligned
ring.

Resolution	Quantity	Coefficient
Absolute resolution	$\sqrt{\dfrac{\langle y_{co}^2 \rangle}{\langle Y_{BPM}^2 \rangle}}$	0.64
Differential resolution	$\sqrt{\dfrac{\langle \eta_y^2 \rangle}{\langle \Delta Y_{BPM}^2 \rangle}}$	$0.58\,/\delta$
Rotation resolution	$\sqrt{\dfrac{\langle \eta_y^2 \rangle}{\langle \Theta_{BPM}^2 \rangle}}$	$0.72\,\mathrm{m}$

be nonzero. When those values were used to correct the ring, vertical dispersion
would be introduced.

Each of the three detector resolution parameters is considered in Fig. 4.2.
We start with a ring with no misalignments and simulate how much orbit or
dispersion is generated solely due to BPM resolution. The ratios from the linear
fit are shown in Table 4.1. In each case, the ratio is smaller than 1, since the
numbers of detectors is sufficient to average out some of the random noise.

4.4 One-Parameter Correction Sequence

The first correction sequence we study corrects one lattice parameter at a time
in three stages. First, the orbit is measured and corrected using vertical steer-
ing magnets. Then the dispersion is measured and corrected, also with vertical
steerings. Finally, the coupling is measured and corrected with skew quads.
Recall from Chapter 3 that we assume the phase has already been corrected.
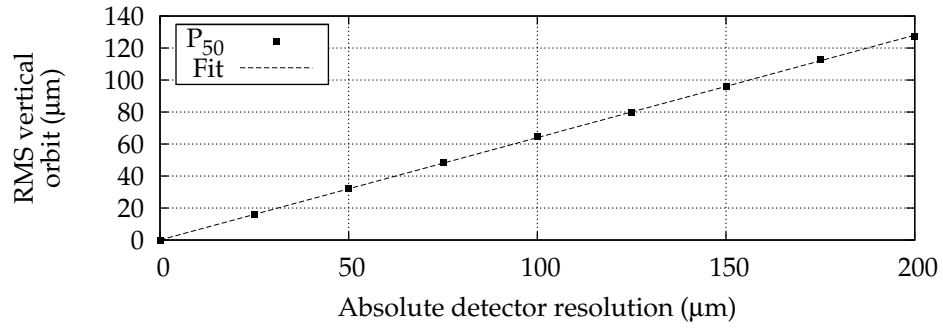
(a) Absolute resolution
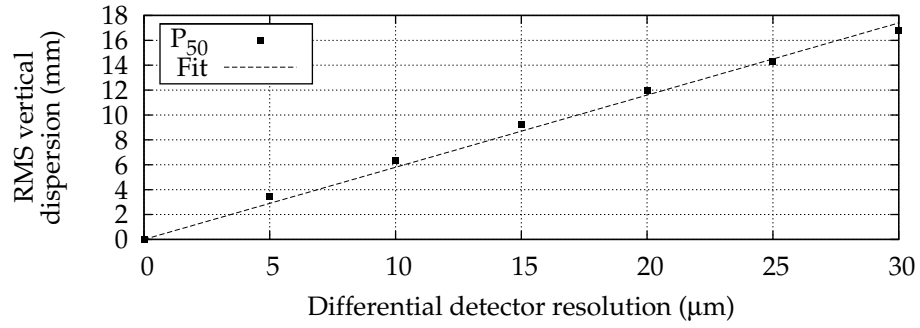
(b) Differential resolution
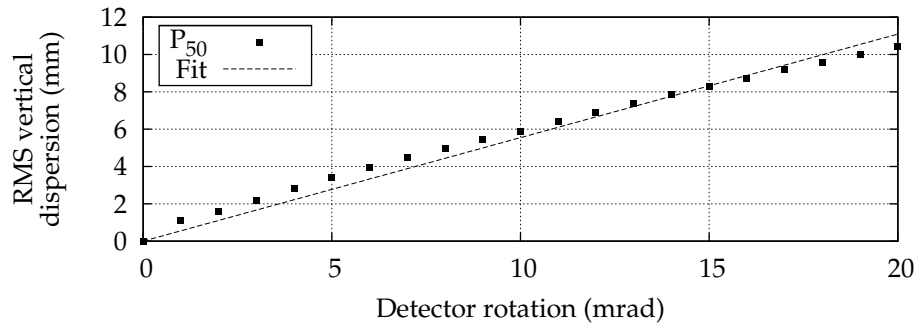
(c) Rotation resolution

Figure 4.2: BPM resolution fits. The coefficients from these fits are shown in Table 4.1.

51

Table 4.2: Misalignment and BPM resolution scenarios.

Scenario	Misalignment	Absolute Resolution (μm)	Differential Resolution (μm)	Rotation (mrad)
1	1× nominal	0	0	0
2	1× nominal	10	2	1
3	1× nominal	50	10	2
4	1× nominal	100	30	2
5	2× nominal	0	0	0
6	2× nominal	10	2	1
7	2× nominal	50	10	2
8	2× nominal	100	30	2

At each stage, we use uniform weights on all detectors and on all corrector elements, so at each stage, there are two parameters that control the optimization. Since the χ^2 from Eq. 4.1 is linear in the weights, the location of the minimum depends only on their ratio. To determine which combination of weights yields the lowest corrected emittance, we fix one weight and vary the other. In this case (and all cases that follow), we will assume that the weight on the changes in the corrector elements is equal to 1.

When optimizing the weights, we look at eight scenarios for misalignment and BPM resolution. These are shown in Table 4.2. Of these, scenario two is considered nominal.

Figure 4.3 shows the weight scan for each of the three stages in the one-parameter correction sequence. The minimum at each stage is used in the subsequent stage(s). One sees that when the weight on the measurement is small (left side of the plots), the optimizer makes no changes to the correctors and simply reproduces the minimum emittance from the previous plot.
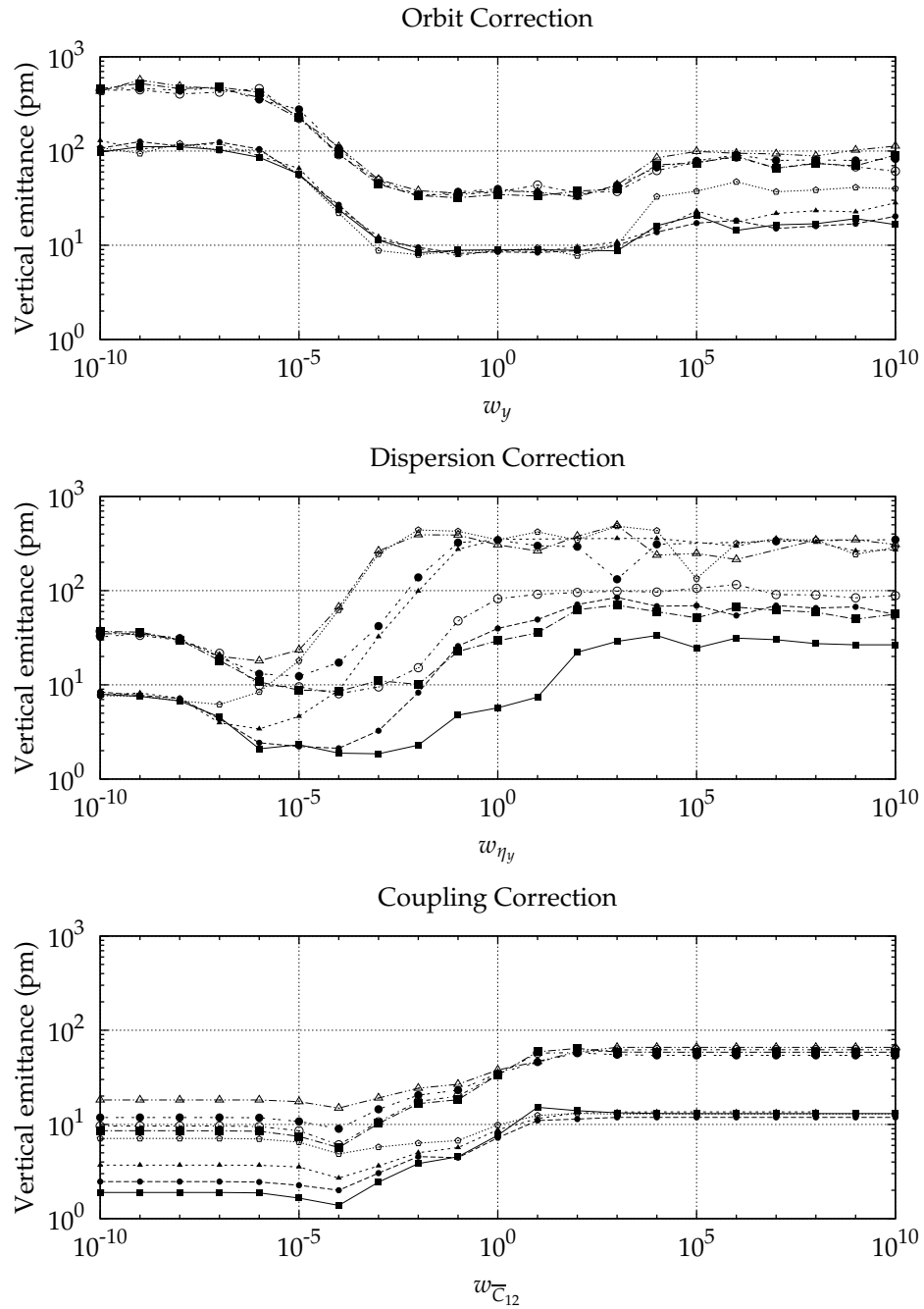
Figure 4.3: Weights for one-parameter correction. The optimum weight for each scenario (each curve) is carried forward. Therefore, the minimum on one plot is equal to the left-most value on the following plot.

Table 4.3: Optimized weights for the one-parameter correction for CesrTA.

Scenario	w_y	Orbit Correction ϵ_y (pm) P_{50}	P_{95}	w_η	Dispersion Correction ϵ_y (pm) P_{50}	P_{95}	$w_{\overline{C}_{12}}$	Coupling Correction ϵ_y (pm) P_{50}	P_{95}
1	1	8.5	20.9	10^{-4}	1.8	7.1	10^{-4}	1.4	4.3
2	1	8.6	20.9	10^{-5}	2.1	7.7	10^{-4}	1.7	4.6
3	1	8.4	21.4	10^{-6}	3.3	9.6	10^{-4}	2.4	6.0
4	1	8.5	21.4	10^{-7}	6.6	15.0	10^{-4}	4.8	11.5
5	1	37.5	98.9	10^{-4}	8.5	39.9	10^{-4}	5.8	21.7
6	1	37.5	99.0	10^{-4}	8.8	42.9	10^{-4}	6.0	22.1
7	1	37.5	99.5	10^{-5}	11.0	49.1	10^{-4}	8.4	24.0
8	1	37.7	98.2	10^{-6}	18.2	61.7	10^{-4}	13.7	32.4

On the other hand, when the weight on the measurement is large (right side of the plot), the emittance is somewhat higher than the minimum. There are at least two likely causes for this behavior. The first is that the optimizer is not guaranteed to find a global minimum (in fact, no such general optimizer exists). By limiting the weight on the measurement, the weight on the corrector changes has more effect, keeping the optimizer from wandering too far and becoming stuck in a local minimum. The second reason is that as the random BPM errors become larger, the measurement becomes less physical and more difficult for the model ring to reproduce. Keeping the corrector changes small helps filter out some of this randomness. In the dispersion measurement, where BPM errors have the most impact, it is quite clear that the optimum weight on the measurement gets smaller as the BPM errors get larger.

Figure 4.4 shows the distribution of random seeds after each stage of the correction for scenario #2 (nominal).
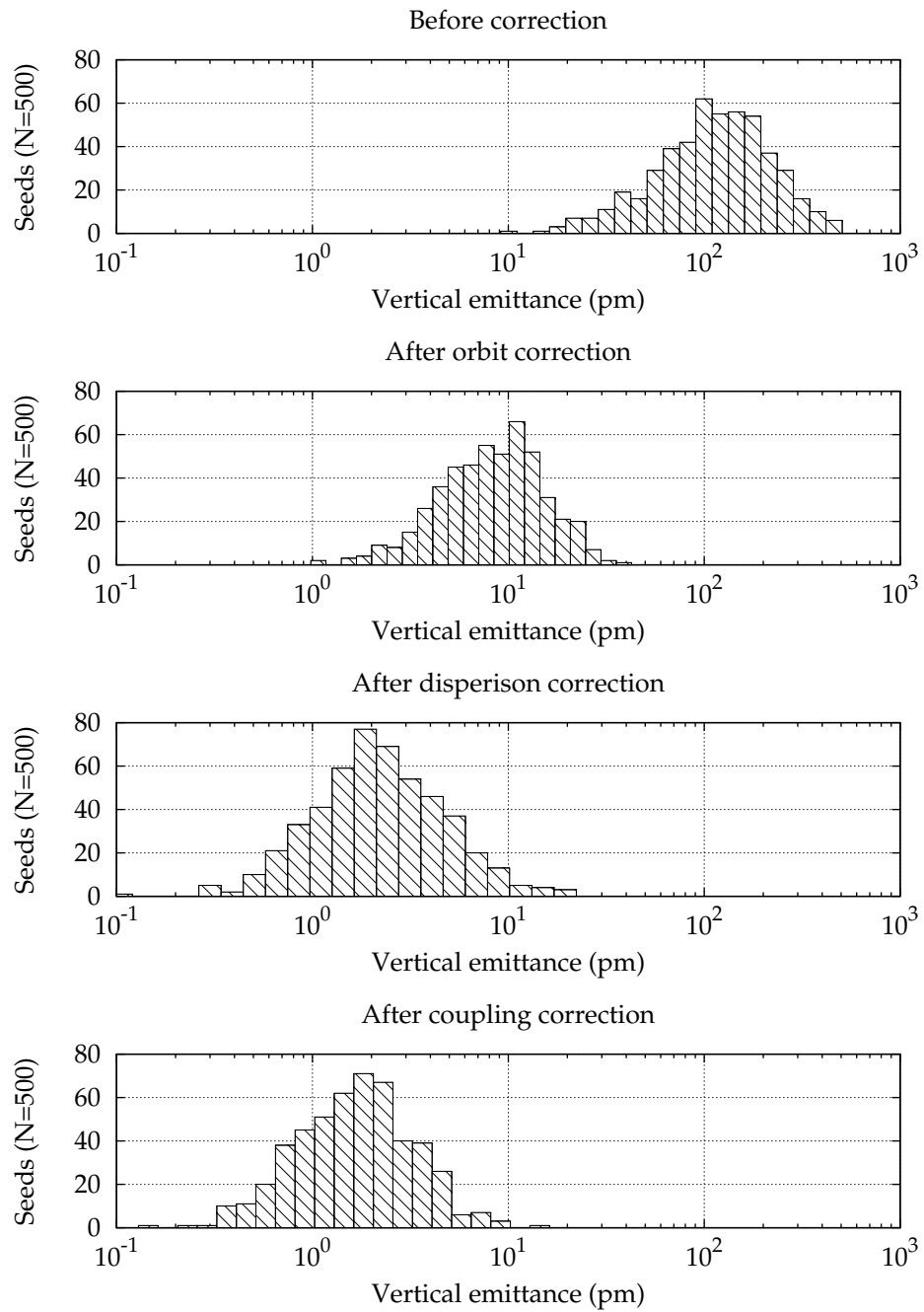
Figure 4.4: One-parameter correction histogram.

The results from the optimized one-parameter correction are shown in Table 4.3. For the scenarios we consider, magnet alignment is far more important than BPM resolution in achieving the desired vertical emittance. Even for the worst-case resolution, we achieve 11.5 pm emittance 95% of the time–just slightly higher than the CesrTA target emittance.

4.5 Two-Parameter Correction Sequence

We can also study a two-parameter correction where two lattice functions are corrected simultaneously. This requires two passes, with the orbit and dispersion corrected in the first pass using vertical steerings, then the dispersion and coupling are corrected in the second pass with the skew quads.

There is a constraint on the changes in the corrector elements, giving a total of three parameters to optimize at each stage. Just as in the one-parameter correction, we are free to fix the weight on the correctors, which we set equal to one. The space of the remaining two parameters is a plane, so the optimization is much more time consuming. However, this only needs to be done once for a given set of misalignments and BPM resolutions, and would not necessarily be slower than the one-parameter correction in practice.

Figures 4.5 and 4.6 show the optimization of the two stages of the two-parameter correction. For each pass, a coarse lattice was scanned first, then a small region near the minimum was scanned with a finer lattice. The resulting optimized weights and corrected emittances are summarized in Table 4.4.
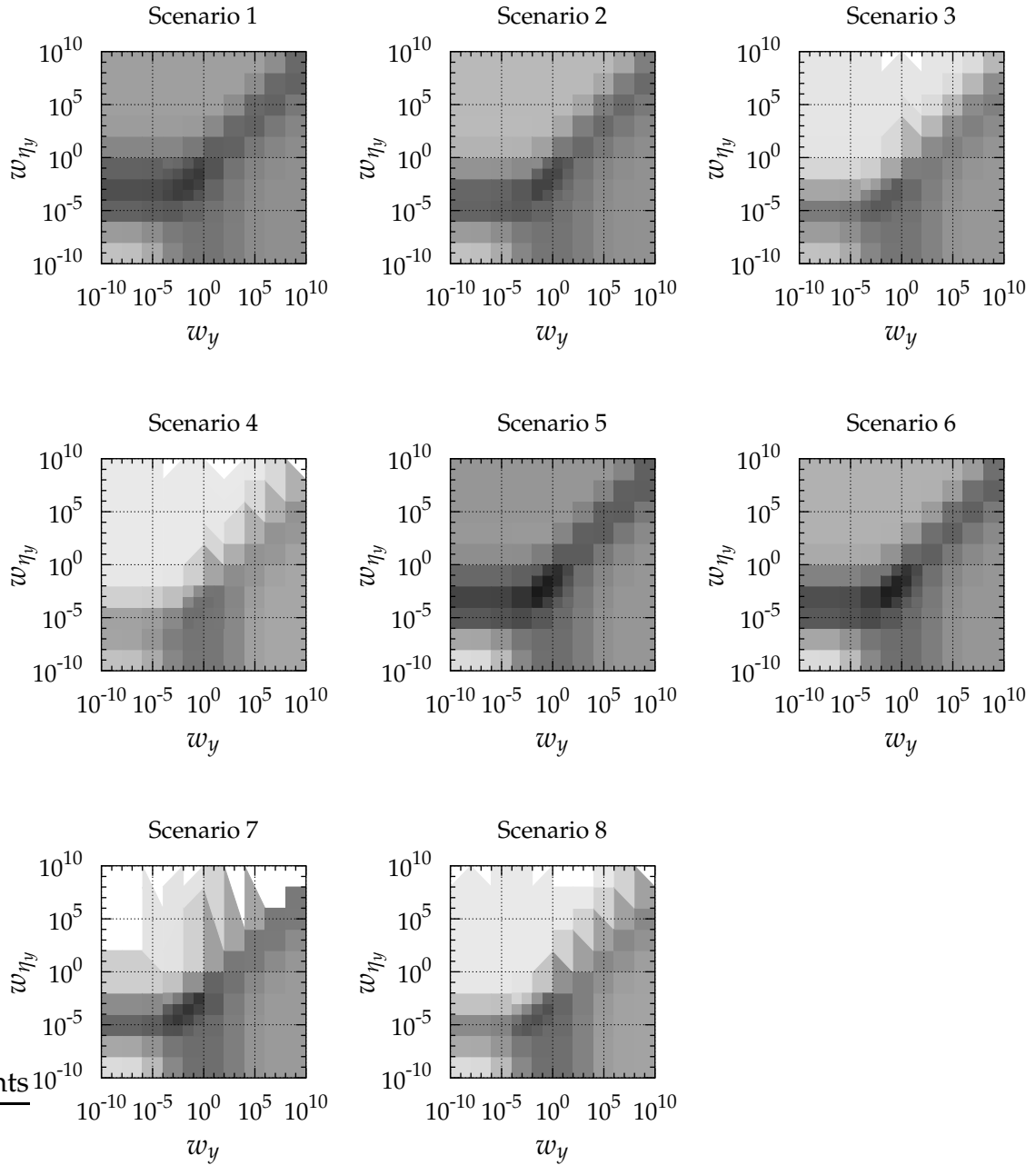
Figure 4.5: Two-parameter optimization of orbit and dispersion.
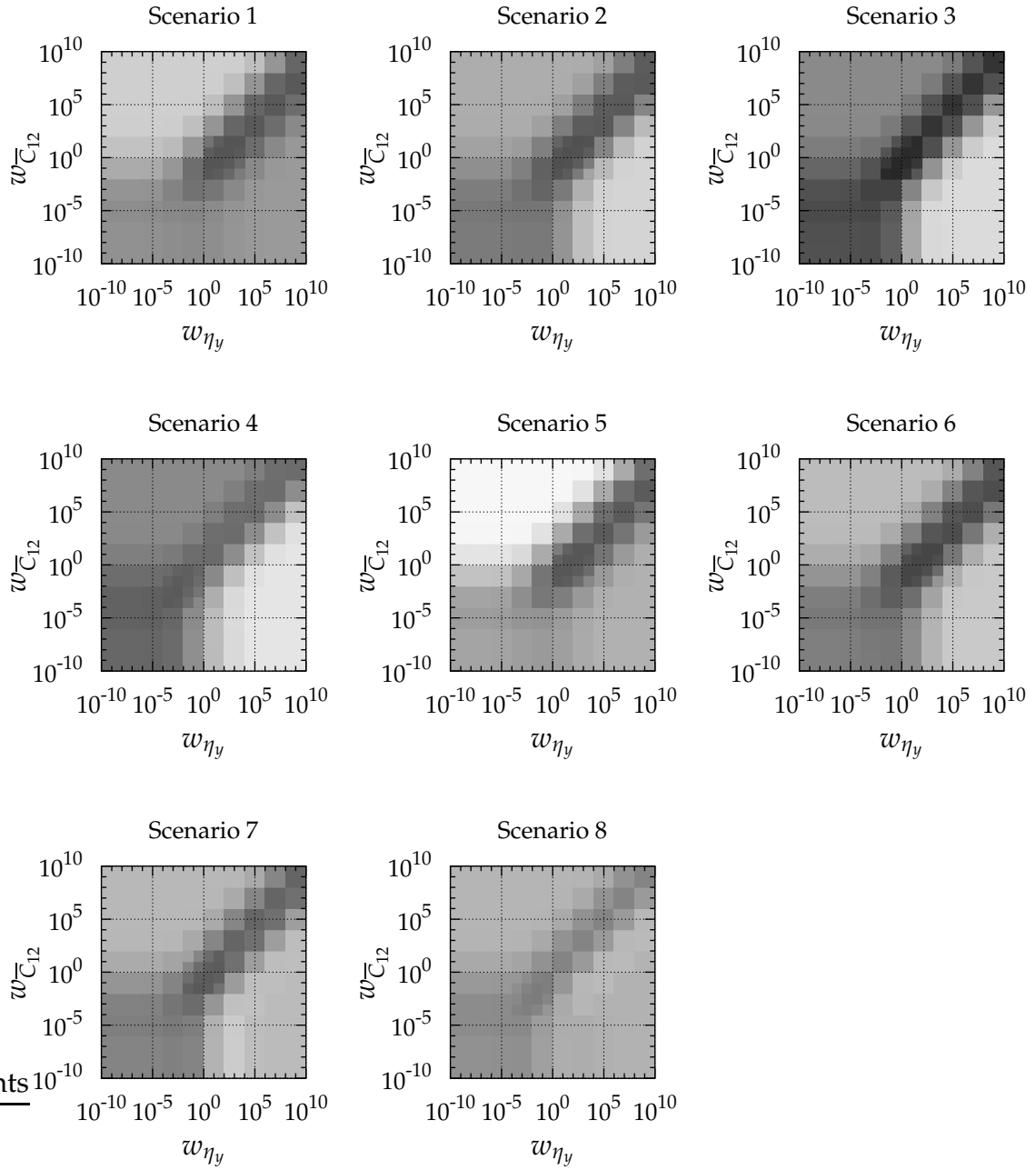
Figure 4.6: Two-parameter optimization of dispersion and coupling.

Table 4.4: Optimized weights for the two-parameter correction for CesrTA.

| | Orbit-Dispersion Correction | | | | Dispersion-Coupling Correction | | | |
| | | | ϵ_y (pm) | | | | ϵ_y (pm) | |
Scenario	w_y	w_{η_y}	P_{50}	P_{95}	w_{η_y}	$w_{\overline{C}_{12}}$	P_{50}	P_{95}
1	10^{-1}	10^{-2}	1.9	6.2	10^2	10	0.4	1.4
2	10^{-2}	10^{-3}	2.2	7.0	10	1	0.5	1.7
3	10^{-2}	10^{-4}	3.5	9.6	10^{-1}	10^{-1}	1.4	3.9
4	10^{-2}	10^{-5}	5.9	15.0	10^{-3}	10^{-3}	3.8	9.6
5	10^{-1}	10^{-2}	10.8	42.5	10^3	10^2	2.4	18.8
6	10^{-2}	10^{-3}	10.8	42.9	10^3	10^2	2.7	18.0
7	10^{-1}	10^{-3}	13.4	48.3	10^{-1}	10^{-2}	4.1	17.8
8	1	10^{-3}	19.4	55.0	10^{-2}	10^{-3}	9.6	24.3

4.6 Summary

We have shown that, for the nominal misalignments and BPM resolution, a one-parameter optimization for the

$$\text{orbit} \rightarrow \text{dispersion} \rightarrow \text{coupling}$$

sequence is sufficient to achieve the target vertical emittance at the 95% level. We can also tolerate significantly worse BPM errors and remain close to our emittance target, again at the 95% level.

   We have also shown that a two-parameter correction for the

$$\text{orbit/dispersion} \rightarrow \text{dispersion/coupling}$$

sequence is more effective, sometimes by more than a factor of two (depending on parameters).

For both correction sequences, however, when misalignments are increased by a factor of two (in Scenarios 4-8), our 95% confidence limit exceeds our emittance targets. We conclude, therefore, with the statement that, for the ranges of parameters considered, achieving the specified alignment is much more critical than achieving the specified BPM resolution.

Chapter 5
ILC Damping Ring

In this chapter, we describe the ILC damping ring, and apply the correction algorithms developed in the previous chapter to it.

5.1   Design

In the ILC the beams coming from the sources (particularly from the positron source) have large emittances. The damping rings reduce the size of the beams before their injection into the main linacs. The challenge with the ILC damping rings is to do two jobs: accept a huge beam and deliver a tiny one. These jobs are sometimes at odds with one another, for example, with regard to the damping wigglers. A larger physical ring helps capture more of the incoming beam, but increasing the vertical gap in the wigglers degrades field quality and may degrade the dynamic aperture.

In its present configuration, the ILC has two damping rings, one for electrons and one for positrons. The rings are stacked vertically in the same tunnel, located near the interaction point.

After the consideration of many different designs, a reference lattice has been agreed upon which has the required acceptance and emittance [25, 26]. General parameters for the damping rings are shown in Table 5.1. Most important for these studies is the desired vertical emittance of 2 nm, which achieves the desired emittance of 0.04 μm (normalized) at the IP, with an emittance growth budget of 100%.

However, the current lattice file does not contain explicit beam detectors or vertical correctors. For this study, the following guidelines are used for positioning those elements:

- One detector for each quadrupole (748 total). Our simulations assume measurements (orbit, dispersion, coupling) are made at the end of each physical quad.[1]

- One skew quad for each sextupole pair (240 total). Horizontal sextupoles are given skew quad components. This gives two skew quads per arc cell.

- Approximately one vertical steering per arc cell or wiggler section, with additional steerings in straight sections and transitions (154 total). Zero-length vertical steerings are added manually to the lattice file at reasonable locations. These are the only elements added to the lattice itself, and are also the least specified at this point in the lattice design process.

The shape of the ring, indicating the the locations of added vertical steerings, is shown in Fig. 5.1.

5.2 Sensitivities and Misalignments

In our examination of emittance correction in CesrTA, we used the estimated survey accuracy to provide initial misalignments for the magnets. Those specifications are not available for the ILC damping rings, but studies have been done to determine the ILC's *sensitivity* to misalignments, i.e., the level of misalignment below which no correction is necessary [27, 28]. Those values are shown in Table 5.2, along with the same quantities for CesrTA and the ATF. For

---

[1]There is an accidental double-counting of the half-quad at the beginning/end of the ring; the prescribed number of detectors is actually 747.
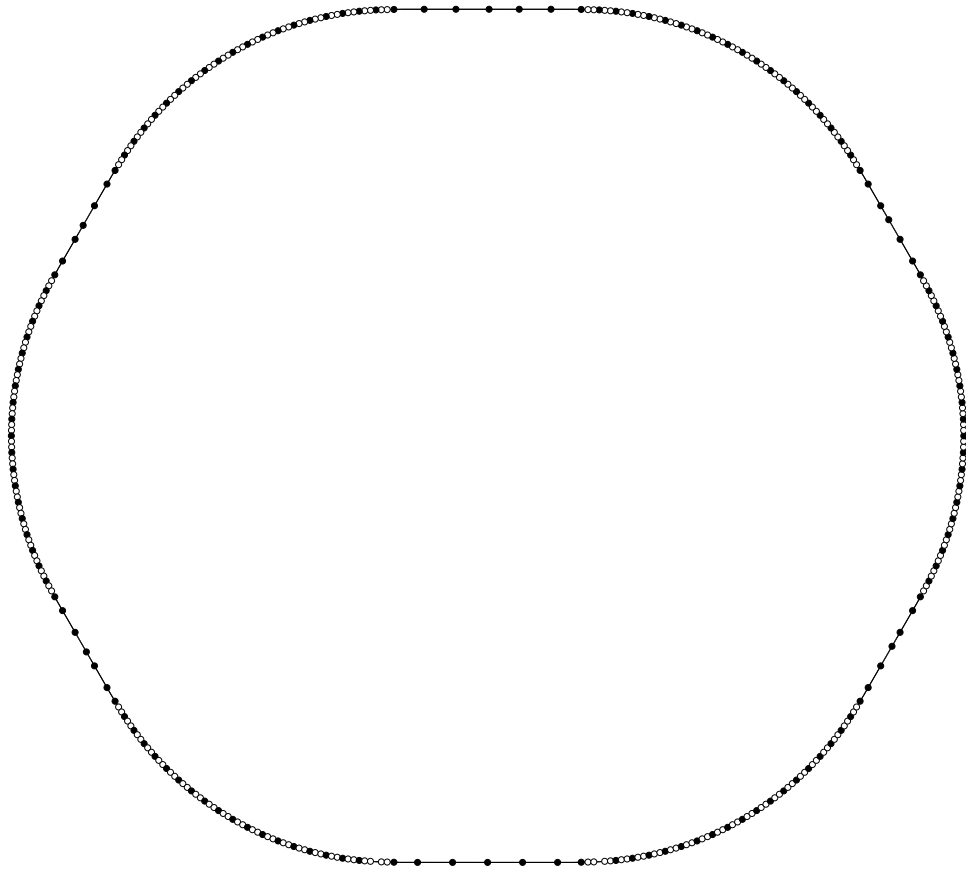
Figure 5.1: ILC damping layout. The locations of vertical steerings and skew quadrupoles are shown with black and white dots, respectively.

Table 5.1: ILC Damping Ring Parameters. The value quoted for ϵ_y is the target emittance after correction. The other values are properties of the lattice.

Parameter	Units	Value
Energy	GeV	5.0
Circumference	km	6.695
Nominal # of bunches		2625
Nominal bunch population		2.0×10^{10}
Average current	A	0.40
Energy loss per turn	MeV	8.7
Beam power	MW	3.5
Nominal bunch current	mA	0.14
RF frequency	MHz	650
Total RF voltage	MV	24
Transverse acceptance, $A_x + A_y$	mm	9
Equilibrium emittance, ϵ_x	nm	500
Equilibrium emittance, ϵ_y	nm	2
Chromaticity, ξ_x, ξ_y		-63/-62
Partition numbers, $\mathcal{J}_x, \mathcal{J}_y, \mathcal{J}_E$		0.9998/1.0000/2.0002
Harmonic number, h		14,516
Synchrotron tune, ν_s		0.067
Synchrotron frequency, f_s	kHz	3.0
Momentum compaction, α_c		4.2×10^{-4}
Betatron tunes, ν_x, ν_y		52.40/49.31
Bunch length, σ_z	mm	9.0
Energy spread, σ_p/p		1.28×10^{-3}
Transverse damping time, τ_x	ms	25.7
Longitudinal damping time, τ_s	ms	12.9

Table 5.2: ILC sensitivities. Other values are shown for comparison, including CesrTA at 2 and 10 pm.

Parameter	ATF	OCS6	CesrTA	CesrTA
Target vertical emittance (pm)	4.5	2	2	10
Orbit amplification factor	20.6	31.6	13.1	
Quadrupole roll (μrad)	582	78.3	153	342
Sextupole alignment (μm)	34.8	67.1	159	356

CesrTA, sensitivities are shown for both 2 pm (the ILC target), and for 10 pm (the CesrTA target).

Because CesrTA has many fewer elements than the ILC damping ring, it has a smaller orbit amplification factor, and larger misalignment tolerances (refer to Eqs. 2.38-2.40). It is also important to note these are isolated misalignments for comparison among the various rings. Since the physical rings have many other misalignments (including quadrupole offsets, which are the most problematic), these figures do not literally mean that no correction will be required.

It is reasonable to estimate that the actual survey accuracy for the ILC will be somewhat better than for CesrTA (since the survey and magnet alignment systems will be more advanced) and somewhat worse than the estimated sensitivity (since doing better than the sensitivity would be inefficient). For our study, however, we simply assume that the ILC will have the same misalignments and identical detector resolutions as CesrTA. The only difference is that, because the OCS lattice file specifies wigglers as individual dipoles, wigglers are not misaligned.

5.3 Correction

Since low-emittance tuning for the ILC damping ring is a global effort, it is worth putting our results in context. We briefly discuss two prominent alternatives before presenting results from CesrTA-style emittance correction.

5.3.1 Other Approaches

First, recall briefly that our correction algorithm uses single measurements to fit a model to the measured data (or perhaps two measurements, but of two different quantities). Only then are corrector elements adjusted and all at the same time.

One prominent alternative is the so-called orbit response matrix (ORM), where one uses the ring itself, rather than a model of the ring, to calculate the correction. ORM can also be used to determine the magnet and detector errors themselves, and this will likely be utilized in CesrTA [29]. Our comparison here is with ORM as tool for routine optics correction.

In that case, Typically, steerings are changed, one-by-one, and a new measurement is taken each time. The accumulated data form a matrix from which one extracts the appropriate corrector settings.

Since the ORM uses more data from the physical ring (which has the actual misalignments present), it may be more effective. However, since so many measurements need to be taken under different conditions, it would likely be much more disruptive to the regular operation of the ring. In other words, it would be harder, if not impossible, to perform in the background. Studies done so far consider using ORM on something like a weekly timescale, and show that, for certain parameters, the method does preserve the required emittance [30].

Another prominent alternative comes from a different way of measuring coupling. Recall that our coupling measurement involves shaking the beam and measuring the resulting amplitude and phase. A simpler approach is to use horizontal steering magnets, and then observe the change in the closed orbit [31]. One can then define the coupling of the ring as

$$C_{xy} = \sqrt{\frac{1}{N} \sum_{\text{steering}} \left(\frac{\sum_{\text{BPM}} (\delta y)^2}{\sum_{\text{BPM}} (\delta x)^2} \right)}.$$

(5.1)

As this is basically just an orbit measurement, it is much simpler than the method we use in CESR. However, it is sensitive to rotation of the steering magnets. It would also be sensitive to BPM rotations, but as we have shown, our measurement is largely insensitive to BPM rotations.

5.3.2 Our Approach

We apply our correction algorithm to the ILC lattice just as we did for the one-parameter case with CesrTA. The ring is corrected with one measurement at a time, applying a new set of corrector settings after each measurement.

The time to fit the model to the measured data scales roughly as the product of number of elements to be varied, times the length of the lattice. If we assume the the density of elements is uniform across different lattices, then in a loose sense, the time to correct the ring scales as the square of the length of the lattice.

Since the ILC damping ring is roughly ten times as large as CesrTA, it is much more time-consuming to perform optimizations with multiple seeds and multiple scenarios. This is not prohibitive in the long run, but until the relevant ILC parameters are better established, it is useful simply to demonstrate that our correction algorithm is effective with some reasonable set of parameters.
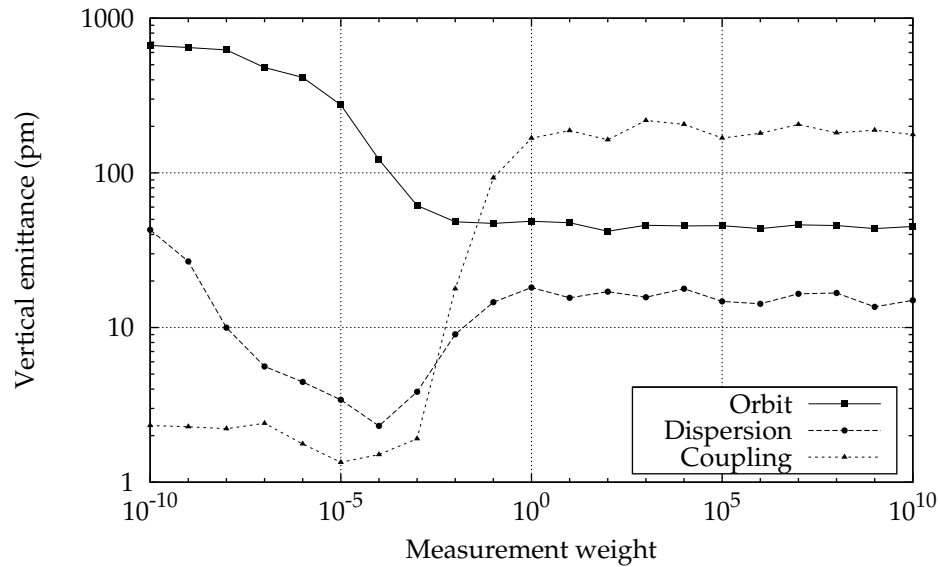
Figure 5.2: Weights for one-parameter correction of the ILC damping ring.

We therefore focus on a single case using the nominal parameters from CesrTA. Generally speaking, these tend to be somewhat worse in terms of misalignment, but somewhat better in terms of BPM resolution, than what some others have used. But again, formal numbers have not been specified.

The optimization of the correction is shown in Fig. 5.2. One sees the same basic features as in the optimization for CesrTA–most notably, that the orbit correction is fairly forgiving for large weights, but that the dispersion and coupling weights require more care to hit the minimum. The emittance after each stage is shown in Fig. 5.3.

The median corrected emittance is 1.3 pm, shown in Table 5.3. This is roughly half of the target of 2 pm, and comparable to results achieved with the ORM method (see references above).
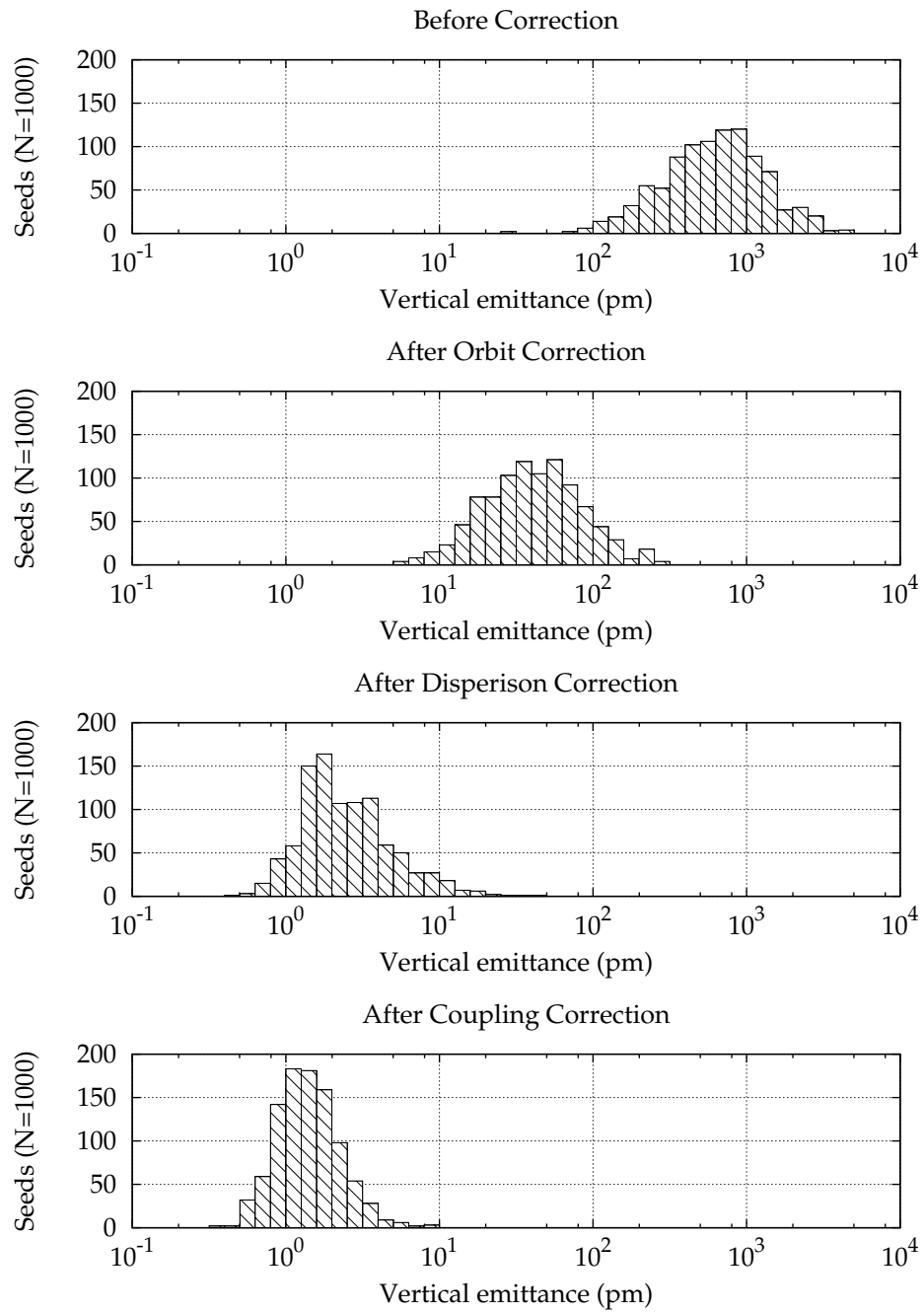
Figure 5.3: Seeds from ILC one-parameter scan.

Table 5.3: Results of one-parameter correction for the ILC damping ring

Correction	Weight Parameter	Weight value	ϵ_y (pm) P50	P95
Before correction			664	1847
After orbit correction	w_y	1	43.6	121
After dispersion correction	w_{η_y}	10^{-4}	2.3	8.3
After coupling correction	$w_{\overline{C}_{12}}$	10^{-5}	1.3	3.0

5.4 Summary

Because the ILC damping ring (and the project in general) is at a relatively early stage, we have made important assumptions in our simulation of emittance correction. We have added detectors and correctors to the lattice at locations consistent with the description in the RDR. Eventually, these will be specified precisely, but this is unlikely to have any significant impact on the correction results.

We have also assumed misalignments and BPM resolutions will be comparable to CesrTA, and while we have argued that these assumptions are reasonable for the time being, it is quite possible that the ILC will do better. In any case, a change in these assumptions would certainly change the emittance results.

Based on our assumptions, we have shown that our algorithm achieves the target emittance. With further study in CesrTA, this correction algorithm can be a significant tool for the ILC, perhaps in lieu of, or at least in addition to, the other techniques discussed.

Chapter 6
Fast Dispersion Measurement

Previous chapters have emphasized the fact that achieving low emittance in a damping ring requires diligent control of the vertical dispersion. This chapter describes the current technique for dispersion measurements at CESR, and proposes a new technique that may prove advantageous for CesrTA and the ILC.

6.1 Motivation

In a scenario like CesrTA or the ILC, we would like to be able to measure the vertical dispersion accurately and often. Accuracy is obviously important because of the potential impact that the vertical dispersion will have on the vertical emittance. Even small amounts of incidental dispersion, arising purely from deviations from the design, can be crippling.

The need to measure the vertical dispersion often comes from the fact that damping rings are not static: magnets move, power supplies drift, etc. For example, it has been observed at CESR that quadrupoles move by an appreciable amount in response to the current in the ring.

Ideally, we would like the ability to measure the dispersion with minimal disruption to the normal operation of the damping ring, allowing frequent, or even continuous, monitoring and correction. This section describes a dispersion measurement technique that addresses this goal along with results obtained at CESR, and comparisons with the conventional method of measuring dispersion.

6.2 Background

In a damping ring, we can calculate a *closed orbit* that is the unique trajectory that closes on itself after one complete revolution. This trajectory will depend on the energy of the particle. Suppose we calculate two closed orbits: one for a particle with the design energy E_0, and another for a particle whose energy differs by a small amount ΔE (small enough that the transport around the ring remains linear). The off-energy orbit will have some transverse displacement relative to the on-energy orbit, and the amount of displacement will be proportional to ΔE, and to the dispersion function $\eta(s)$, where s is the longitudinal position.

In the horizontal case, the displaced orbit at s is given by

$$x(s) = x_0(s) + \frac{\Delta E}{E_0} \eta_x(s) \tag{6.1}$$

where x_0 is the on-energy closed orbit. From Eq. 6.1, we define the dispersion as

$$\eta_x(s) \equiv \frac{\Delta x(s)}{\Delta E / E_0}. \tag{6.2}$$

The vertical situation is mathematically identical, but it is of some practical importance to remember that η_y is usually zero by design, and that typically, $\eta_y \ll \eta_x$.

An important consequence of dispersive orbit distortion is that particles with different energies will have different path lengths as they curve through bending magnets. The change in path length ΔL is described by the *momentum compaction* and is given by

$$\alpha_c = \frac{\Delta L / L_0}{\Delta E / E_0} = \left\langle \frac{\eta_x}{\rho} \right\rangle \tag{6.3}$$

where L_0 is the unperturbed circumference of the ring, ρ is the radius of curvature, and the average is taken around the ring.

6.3 RFFM Measurement Technique

The simplest dispersion measurement is to record two orbits at two slightly different energies. The difference in those orbits at each location, scaled by the energy difference, gives the dispersion at that location according to Eq. 6.2.

For such a measurement, the energy of the beam is changed by changing (modulating) the frequency of the accelerating RF cavities, hence the abbreviation *RFFM*. Adjusting the cavity frequency causes the beam to come to a new equilibrium energy that preserves the synchronous phase condition between the arrival time of the beam and the oscillation of the RF wave. The relationship between RF frequency f and beam energy is given by

$$\frac{\Delta E}{E_0} = -\frac{\Delta f}{f_0} \cdot \left(\alpha_c - \frac{1}{\gamma^2} \right)^{-1} \tag{6.4}$$

where γ is the relativistic factor. Electron damping rings operate well above transition energy where $\gamma^2 \gg \frac{1}{\alpha_c}$, so the relativistic factor can be safely ignored.

Equation 6.4 uses α_c to calculate the dispersion, but α_c itself depends on the dispersion. To avoid this circular dependence, the value of α_c that is used in the dispersion measurement comes from the design lattice, not from an independent measurement. It is assumed, therefore, that even though the dispersion at any given detector may deviate from the design, those deviations average out and are not reflected in the value of α_c. This assumption will be explored further in a subsequent section.

Two final points should be made about the RFFM measurement that help motivate the improved technique that will be presented next. First, changing the RF frequency affects every bunch in the ring. This is not necessarily a problem in the CesrTA context where the low emittance beam will be stored for a relatively long time. However, in an ILC damping ring, bunches are stored only until they reach their target emittance, then sent down the linac for high-luminosity

collisions. Disturbing every bunch in the ring, while perhaps not disastrous, is clearly a disadvantage.

Second, the time that is required for the RF modulation is on the order of minutes. This makes frequent RFFM measurements impractical, but as stated in the introduction to this chapter, frequent dispersion monitoring may be essential to maintaining low emittance in both CesrTA and in the ILC.

6.4   Fast Measurement Technique

This section introduces a new way of measuring the dispersion that we dub the *fast dispersion measurement*. From the outset, it should be stated that this is an attempt to demonstrate the prospects for a fast dispersion measurement. Some of what is presented here by way of motivation will depend on the particular context, and may or may not be possible in a particular realization of CesrTA or the ILC.

This technique is faster than the RFFM technique at CESR because it does not require changing the RF frequency and it makes use of the faster upgraded BPM system. It is possible that hardware upgrades will remove this advantage–ILC BPMs will certainly be capable of faster measurements.

However, there is still a speed advantage because, under certain scenarios, the fast measurement only requires manipulating the energy of a single bunch. Therefore, the integrated luminosity from the other few-thousand bunches stored in an ILC damping ring will be unaffected. The technique might better be called a *fast/unobtrusive* technique.

6.4.1 Basics of Measurement

The basic idea behind the fast technique is to keep the ring's equilibrium energy constant, and make a bunch oscillate in energy about that equilibrium value. If we simply assume that the energy of the beam has a sinusoidal time-dependence (ignoring the energy lost around the ring and gained at the RF cavities), then modifying Eq. 6.1 to account for that gives a closed orbit that oscillates in time

$$x(s,t) = x_0(s) + \frac{\Delta E_{\max}}{E_0} \cos\left(\omega_E\, t\right) \eta_x(s) \tag{6.5}$$

where $\Delta E_{\max}$ and ω_E are the amplitude and frequency of the energy oscillation, respectively. Thus, we actually measure the dispersion by measuring the fluctuations in the closed orbit.

However, the oscillating closed orbit is somewhat unconventional, and there is no guarantee that a bunch will actually travel on that orbit. To take one extreme, if ω_E is very fast compared with the revolution frequency, then the beam will not have time to respond to the changing RF frequency, and the oscillatory behavior will wash out (if such exotic behavior were actually achievable in the first place).

In reality, there is little flexibility to choose ω_E. The energy of particles in the beam has a natural oscillation frequency determined by the strength of the phase-focusing from the accelerating RF. That frequency, called the synchrotron frequency, is given by

$$\Omega = \omega_{\text{rev}} \sqrt{-\frac{e\, V_0\, h\, \cos\Psi_0}{2\pi\, \beta^2\, E_0} \left(\alpha_c - \frac{1}{\gamma^2}\right)} \tag{6.6}$$

where ω_{rev} is the revolution frequency, V_0 is the peak RF voltage, $h = \frac{\omega_{\text{RF}}}{\omega_{\text{rev}}}$ is the harmonic number, and Ψ_0 is the synchronous RF phase. There are numerous practical limitations to inducing energy oscillations at a frequency other than

75

Ω, even if it were possible in principle. Those limitations would generally be at odds with our goal of providing an unobtrusive measurement technique, so we will assume that $\omega_E = \Omega$ in all cases.

Fortunately, in nearly every conceivable case, $\Omega \ll \omega_{\text{rev}}$, so that a complete energy oscillation requires many trips around the machine. Moreover, the dispersion changes on approximately the same length scale as the betatron oscillation, which is generally much shorter than the circumference of any damping ring. Therefore, we are assured that the dispersion function is changing around the ring much faster than the energy of the beam. The statement that $\omega_E = \Omega \ll \nu_x$ is important because it provides a reasonable guarantee that the beam (or at least the average position of the beam) stays on the closed orbit, which is necessary for us to see the behavior described by Eq. 6.5.

We are certainly ignoring many other components of the motion that may be present, for example, coherent betatron motion. However, it will be shown that Eq. 6.5 does provide a model that is realistic enough to extract the dispersion.

6.4.2 Inducing Energy Oscillation

Several potential methods have been suggested for creating energy oscillations in a damping ring:

1. **Injection Energy Offset.** If a bunch is injected into a damping ring with some energy other than the equilibrium energy of the ring, it will oscillate about the equilibrium energy with an initial amplitude equal to the energy mismatch. This could be done by deliberately changing the injection energy for a single bunch, leaving all other bunches untouched.

2. **Injection Transients.** It may be possible to measure injection transients for many bunches without a deliberate energy mismatch, accumulating

enough data after many successive injected bunches to make a meaningful measurement.

3. **Pulsed Longitudinal Bump.** A pulsed element could provide a longitudinal kick to a single stored bunch.

4. **Pulsed Transverse Bump.** A transverse bump could create a path length difference for a single bunch that would turn into an energy oscillation on successive turns.

For all of the aforementioned approaches, the energy oscillations that are produced will damp down exponentially. The measurement must be conducted before significant damping occurs, or the damping behavior must be accounted for in the subsequent analysis. Another issue is decoherence, where the motion of the individual particles in the bunch oscillate out of phase.

The effects of damping and decoherence limit how long we have to accumulate data once an instantaneous excitation has occurred. If enough data cannot be obtained, then the excitation could be repeated.

6.5 Measurements At CESR

Despite the various proposed techniques for creating energy oscillations, the situation at CESR is presently constrained in a couple of ways. First, although the ILC design specifies injecting the full bunch current in one shot, CESR builds up stored current by injecting many smaller bunches into the same RF bucket. The signal from a single injected pulse is too far below the sensitivity of the BPM system to make meaningful orbit measurements. This rules out using off-energy injection schemes (items 1 and 2).

Second, although the prospects for using pulsed bumps (items 3 and 4) at CESR are better, significant care will need to be taken in the configuration of the bumps themselves so that unwanted transverse motion is not induced. Furthermore, the orbit measurement will need to be synchronized so that the oscillations do not damp or decohere before data can be taken.

The second concern is less fundamental than the first, and it is believed that they can be overcome when sufficient machine time is available. Therefore, it should eventually be possible to use CESR (or in the longer term, CesrTA), to demonstrate the fast dispersion measurement on a single bunch.

6.5.1 RF Phase Modulation

For the time being, we can demonstrate the principle at CESR using phase-modulation of the accelerating RF. Normally, the phase of the RF wave relative to the arrival of a bunch is fixed so that the bunch receives the energy kick necessary to replace the precise amount of energy lost due to damping. If the RF wave is phase-shifted on a turn-by-turn basis, then the bunch will receive some energy kick (positive or negative) relative to its equilibrium, and will tend to oscillate.

Since the beam naturally oscillates at the synchrotron tune, modulating the RF phase at that frequency drives the beam on resonance. This produces energy oscillations that are of sufficient amplitude for this measurement.

Furthermore because we drive the bunch continuously, damping and decoherence are not a factor. The bunch oscillates indefinitely, and there is no need for synchronization of the orbit measurement.

6.5.2 Multiturn Orbit Measurement

Presently in CESR, multiturn measurements are made for 1024 turns at thirteen detectors located near the CLEO interaction point. It is expected that all the detectors in the ring will eventually have this capability.

The multiturn data should have the form of Eq. 6.5. We know the oscillation frequency, $\omega_E = \Omega$, so that expression can be linearized as

$$x(t) = c_1 \cos\left(\frac{\Omega}{\omega_{\text{rev}}} n\right) + c_2 \sin\left(\frac{\Omega}{\omega_{\text{rev}}} n\right) + c_3 \tag{6.7}$$

where ω_{rev} is the revolution frequency and n is the turn number. The same function is fit for both horizontal and vertical motion.

Because the fit is for the fixed, known frequency $\omega_E = \Omega$, the higher frequency motion (including random noise) is effectively filtered out. Figures 6.1 and 6.2 show the horizontal and vertical data and fit from two multiturn measurements at different drive amplitudes (different output levels from the spectrum analyzer). The top plot in each figure corresponds to a -38 dBm drive level, and the bottom to a -18 dBm drive level. For the horizontal data in Fig. 6.1, there is clearly a strong signal at the drive frequency even when the amplitude is relatively low. However, for the vertical data in Fig. 6.2, the top plot shows a very poor signal-to-noise ratio. The signal is not striking in the bottom plot either, but as results will show, it is strong enough to extract the value of the vertical dispersion.

From the fits to the multiturn data, we extract an amplitude and phase according to

$$A_{x|y} = \sqrt{c_1^2 + c_2^2} \tag{6.8}$$

$$\phi_{x|y} = \arctan(c_2, c_1). \tag{6.9}$$
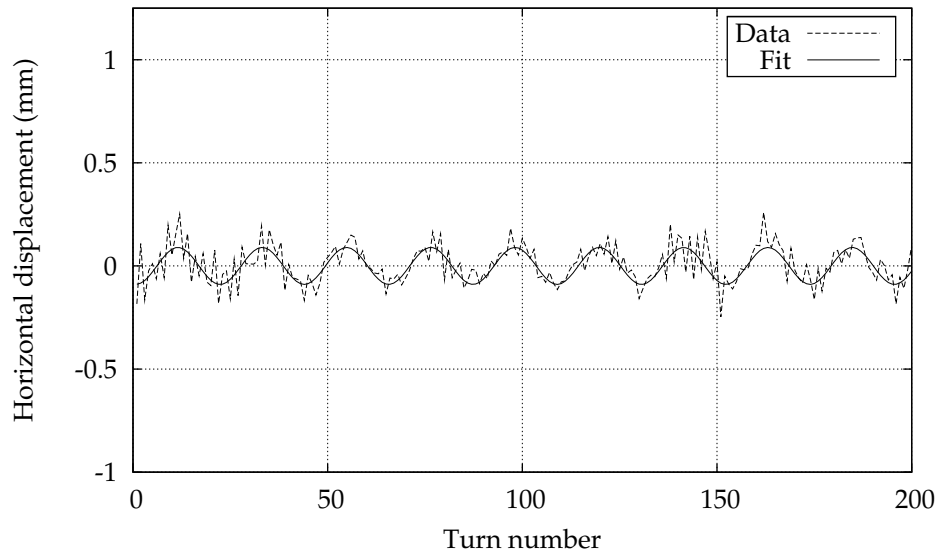
(a) -38 dBm drive
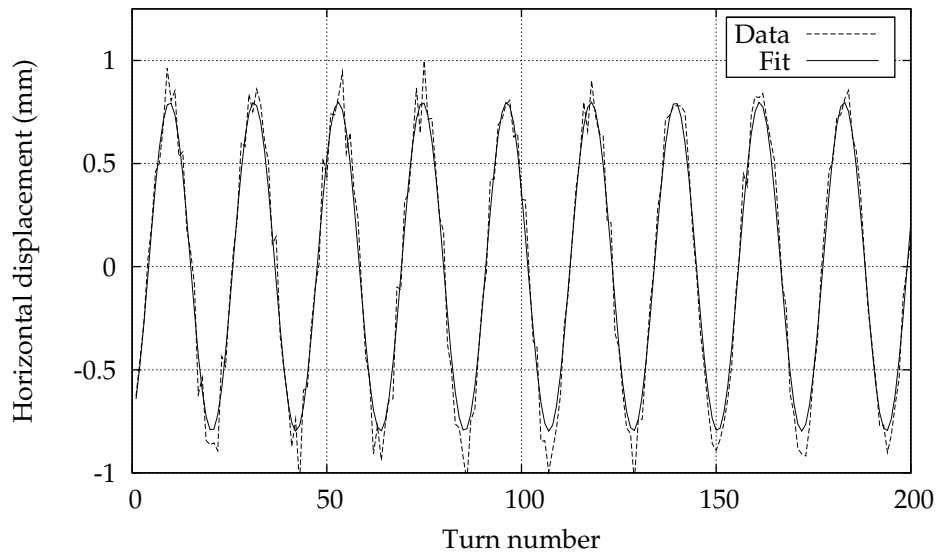
(b) -18 dBm drive

Figure 6.1: Horizontal multiturn data. The horizontal data and sinusoidal fit for the first 200 turns (out of 1024) are shown for detector 9W. At this location, $\eta_x \sim 1\,\mathrm{m}$, which makes the horizontal signal clear, even at the weaker drive.
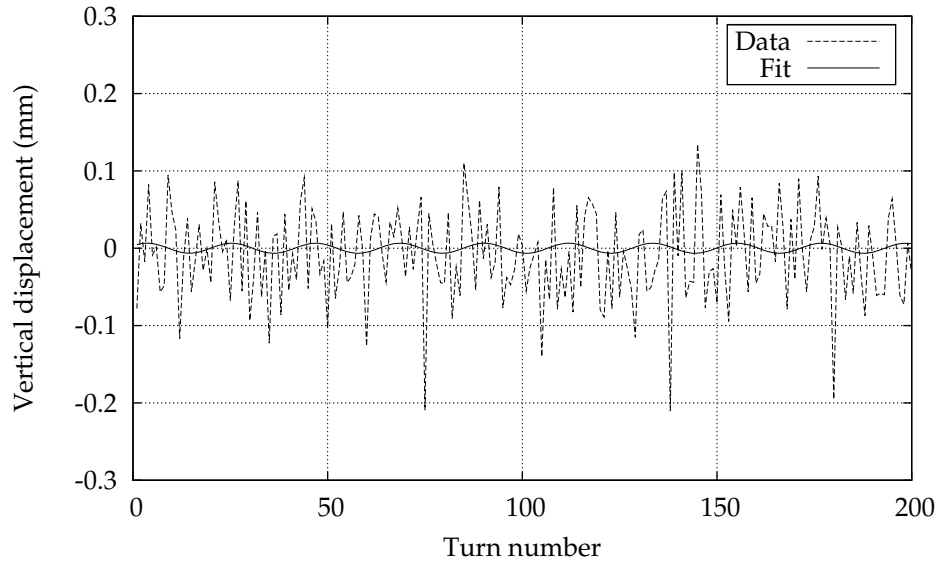
(a) -38 dBm drive
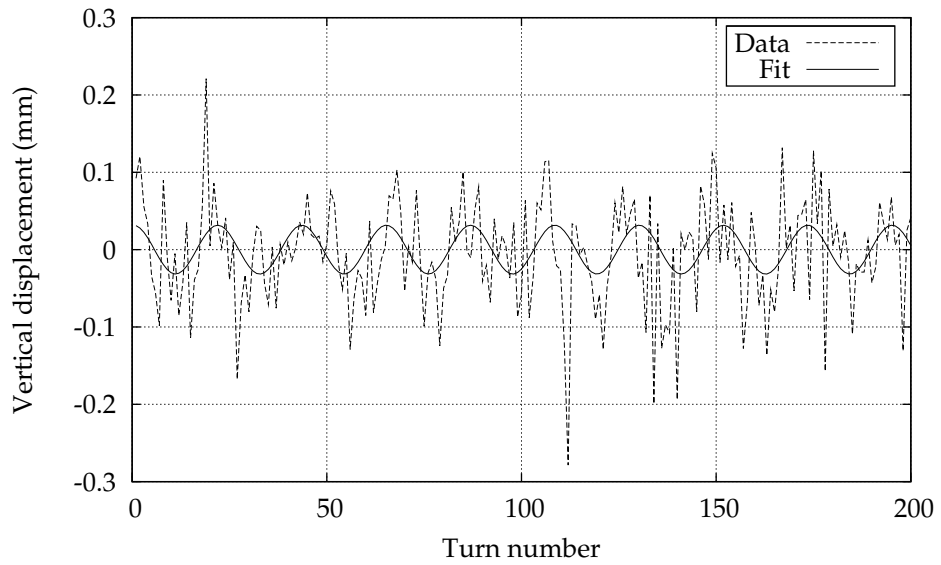
(b) -18 dBm drive

Figure 6.2: Vertical multiturn data. The vertical data and sinusoidal fit for the first 200 turns (out of 1024) are shown for detector 9W. At this location, $\eta_y \sim 5\,\mathrm{cm}$, and the signal-to-noise is much worse than in the horizontal data (Fig. 6.1).

These two parameters determine the measured dispersion, but because of how we are performing the measurement, some further analysis is necessary.

6.5.3 Multiturn measurement phase

The actual dispersion may be positive or negative at a given detector. The measured displacement of the closed orbit is proportional to the dispersion and to the energy deviation, so we need a way to determine the sign of the energy oscillation independently. In other words, we need to know whether the multiturn measurement started when the energy oscillation was positive or negative.

In principle, the measurement could be synchronized with the energy drive, but even without that, we can determine the sign of the dispersion by looking at the phase parameter from Eq. 6.9.

Given that the horizontal dispersion is known reasonably well from the model, we choose the detector with the largest value of η_x and use the phase from that detector as a reference. The phase from every other detector, for both the horizontal and vertical, is compared with the reference. If the two phases differ by less than $\pm\pi/2$, then the two dispersion values have the same sign. If the two phases differ by more than that amount, then their signs are opposite. This is implemented as

$$\text{sign}\,\eta_i = \begin{cases} \text{sign}\,\eta_x^{\text{ref}}, & \cos\left(\phi_i - \phi_{\text{ref}}\right) \geq 0 \\ -\text{sign}\,\eta_x^{\text{ref}}, & \cos\left(\phi_i - \phi_{\text{ref}}\right) < 0. \end{cases} \tag{6.10}$$

6.5.4 Scale Factor

Comparing the fit function to Eq. 6.5, the amplitude of the closed orbit oscillation A is given by

$$A_i = \frac{\Delta E_{\text{max}}}{E_0}\,\eta_i. \tag{6.11}$$

In our measurements, we do not know, a priori, the value of ΔE_{max}. The beam is clearly being driven by the cavities, but by exactly how much is a difficult question. Without ΔE_{max}, we only know the dispersion up to an overall scale factor (a single number for all detectors). Fortunately, we can determine ΔE_{max} by assuming that the mean value of the measured horizontal dispersion is equal to that of the design lattice.

This is a reasonable assumption for two reasons. First, the horizontal dispersion is very large compared to the types of deviations we expect to get from magnet misalignments (of course, this is not true for the vertical dispersion). Second, the deviations that are caused by misalignments are small oscillations about the design value, and tend to average out after a full turn.

This is similar to the assumption used in the conventional measurement, i.e., that the design momentum compaction is unchanged. We merely assume $\langle \eta_x \rangle$ is constant rather than $\langle \eta_x/\rho \rangle$. In Fig. 6.3, different random element misalignments with magnitudes given by the expected values in CesrTA are used to calculate the expected variation in $\langle \eta_x \rangle$. This simulation verifies that the mean value of the horizontal dispersion is stable to approximately 1%.

Under this assumption, we can determine ΔE_{max} from Eq. 6.11:

$$\langle A_x \rangle = \frac{\Delta E_{max}}{E_0} \langle \eta_x \rangle \tag{6.12}$$

$$= \frac{\Delta E_{max}}{E_0} \left\langle \eta_x^{model} \right\rangle \tag{6.13}$$

$$\frac{\Delta E_{max}}{E_0} = \frac{\langle A_x \rangle}{\left\langle \eta_x^{model} \right\rangle}. \tag{6.14}$$

The dispersion at each detector is then given by

$$\eta_{x|y,i} = \frac{A_{x|y,i}}{\Delta E_{max}/E_0} \times (\text{sign from Eq. 6.10}) . \tag{6.15}$$

A final point about the scale factor is that it may not matter very much. In most conceivable applications of this technique, the objective is to reduce the
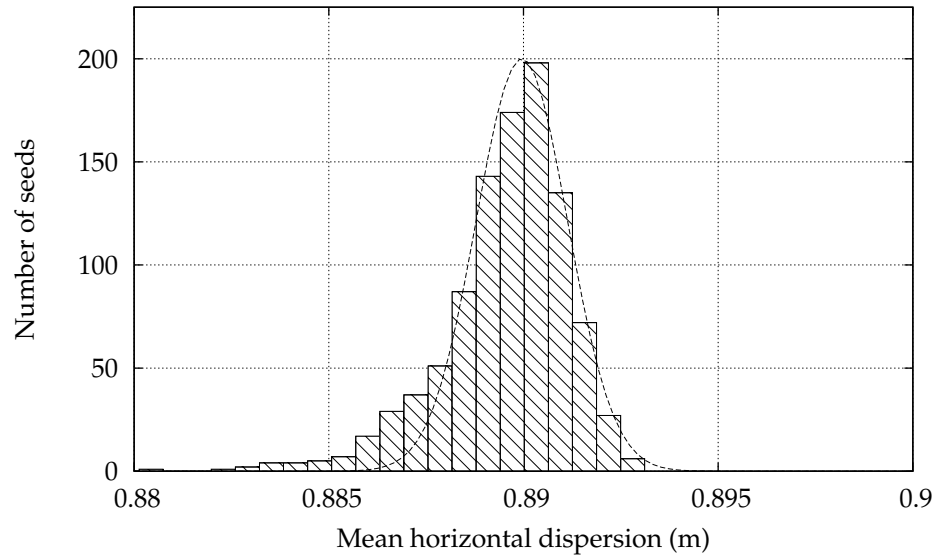
Figure 6.3: Stability of $\langle \eta_x \rangle$. The horizontal dispersion is averaged around the ring for one thousand random seeds with the nominal misalignment parameters. The fit gives a value of $\langle \eta_x \rangle = 0.890 \pm .0012$ m, i.e., $\langle \eta_x \rangle$ is stable to approximately 1%.

vertical dispersion to zero. If there is some error in the scale factor, then the correction will slightly over or undercompensate for the true dispersion. Simply repeating the correction will reduce the error exponentially.

6.6 Results

The fast dispersion measurement procedure has been studied at CESR in several machine studies periods [32, 33, 34, 35]. This section summarizes the last study, from May, 2007.

First, we need to establish criteria for evaluating the fast measurement technique, or put another way, we need something to compare with the fast measurement in order to judge its accuracy. We begin by comparing the fast measurement to the model, and to the RFFM technique.

6.6.1   Comparison with Model

The model dispersion is based on the lattice design, plus the calculated response to whatever changes have been put into the ring at the time the measurement was taken (steering, tuning, etc.). As we have demonstrated, the model value for the horizontal dispersion is relatively reliable, and a direct comparison is appropriate.

The vertical case is different, since the model value is typically small or zero, and unknown factors, such as misalignments, produce vertical dispersion on the scale that we would like to measure. We can, however, use the model to predict *changes* in the vertical dispersion. For example, when a bump is added, it changes the vertical dispersion by a known amount, on top of whatever was there before.

Figure 6.4 shows the horizontal and vertical dispersion as measured with both techniques. The data shows the mean and standard deviation for two measurements of each type. Of course, the standard deviation of two numbers is not of any rigorous statistical value, but it may give some idea of the reproducibility of the two techniques.

In these particular measurements, there was some significant vertical dispersion due to the solenoid compensation for CLEO. In addition, a vertical bump was used in order to generate even more vertical dispersion.

Both techniques indicate strong agreement with the model in the horizontal case. Because of the large horizontal dispersion, we expect that this signal is easy to see by either technique.

For the smaller vertical dispersion, both techniques show poorer agreement with the model. However, for the reasons stated earlier, the vertical model is known to differ from the true dispersion. The agreement between the fast and
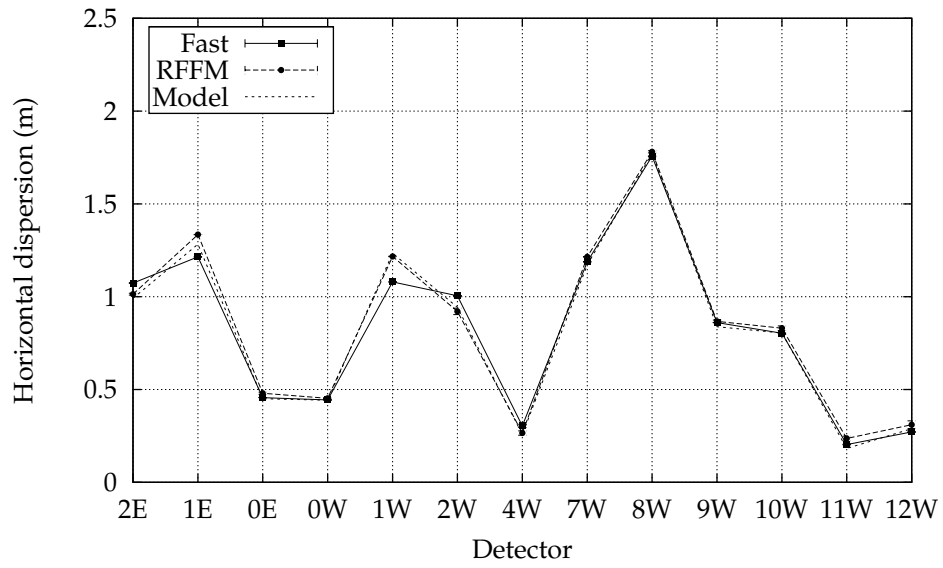
(a) Horizontal dispersion
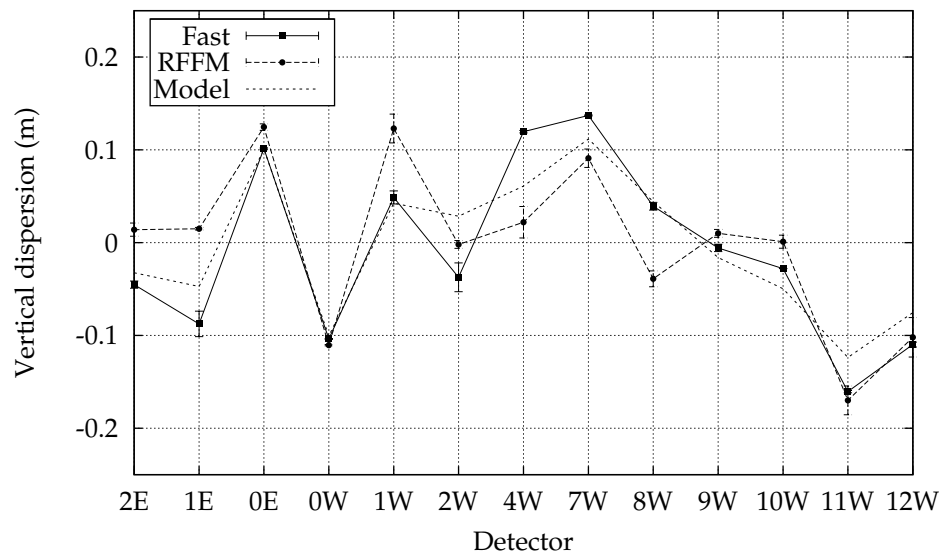
(b) Vertical dispersion

Figure 6.4: Comparison of dispersion measurement for fast and RFFM techniques.

RFFM techniques is also poorer, but the fast technique does show better repro-
ducibility.

Since we believe the model is a better predictor of changes in the vertical dis-
persion, another valuable comparison between the fast and RFFM techniques is
to look at the change with the bump on and off. Figure 6.5 shows the vertical
dispersion for both techniques. Two measurements were taken for each tech-
nique in each bump condition, giving four possible comparisons. The mean and
standard deviation of each possible difference measurement is shown. With the
obvious exception of detector 2W (where the beam pipe is unusually large), the
fast technique is generally in better agreement with better reproducibility.

6.6.2   Energy Amplitude

An important variable in the fast measurement is how hard we should drive
the beam's energy oscillation. When resources are available, a systematic study
is certainly in order. To some degree, this question can be addressed with the
data already taken. A first point to make is that none of the previous machine
studies, which have used fractional energy drive amplitudes between 0.1×10^{-3}
and 1.8×10^{-3}, have shown any appreciable beam loss.

A more subtle question is whether we are introducing any significant nonlin-
earities, either in the transverse motion or in the energy oscillations (which are,
of course, related), that would invalidate our simple model. Figure 6.6.2 con-
tains every horizontal dispersion measurement made using the fast technique.
The vertical dispersion cannot be compared in this way because the vertical
dispersion was not constant (or nearly so) across all of these different measure-
ments. The top plot shows that at each detector, the fit amplitude is proportional
to the $\Delta E_{\max}/E_0$. Since $\Delta E_{\max}/E_0$ is calculated from the fit amplitudes across
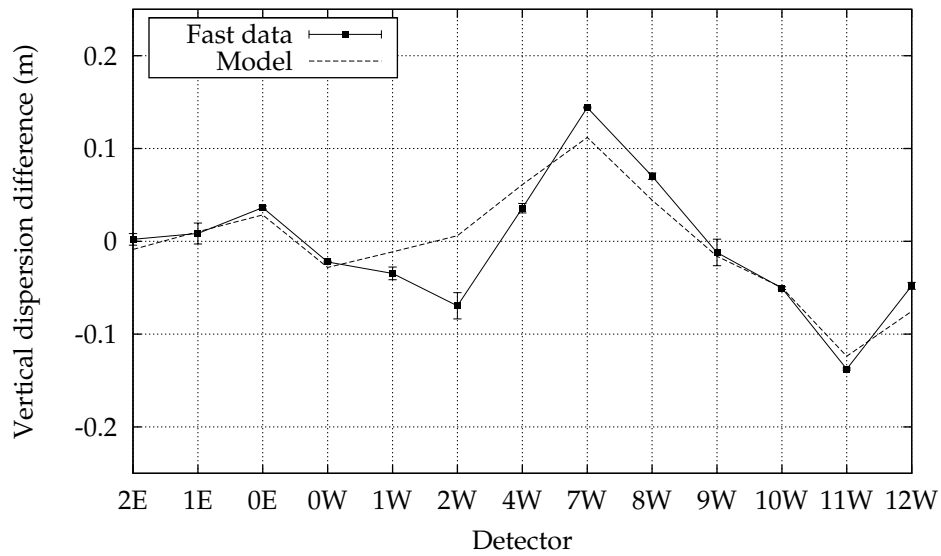
(a) Fast technique
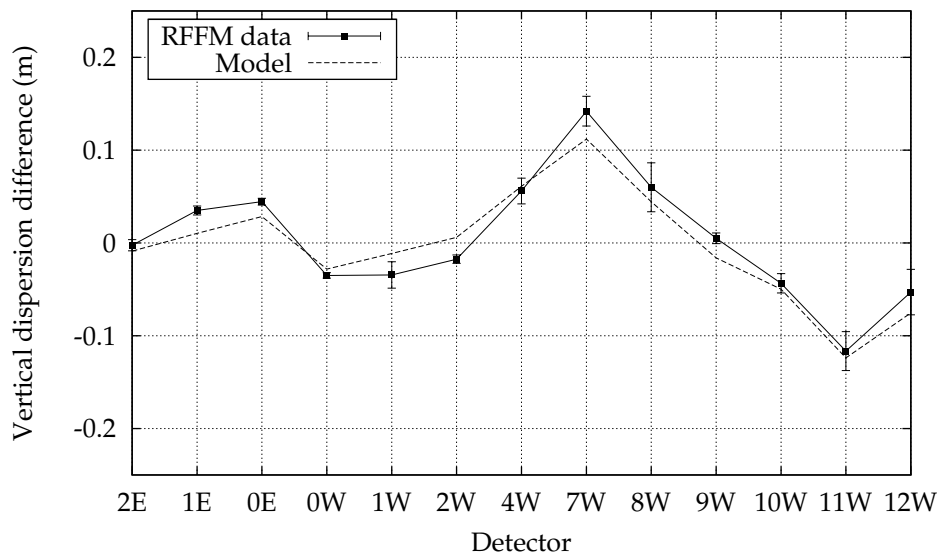
(b) RFFM technique

Figure 6.5: Vertical dispersion difference. Two measurements with the bump on and off (four total) were taken using each technique. The mean and standard deviation of each possible difference is plotted. The fast technique (top) is generally in better agreement with the model dispersion.
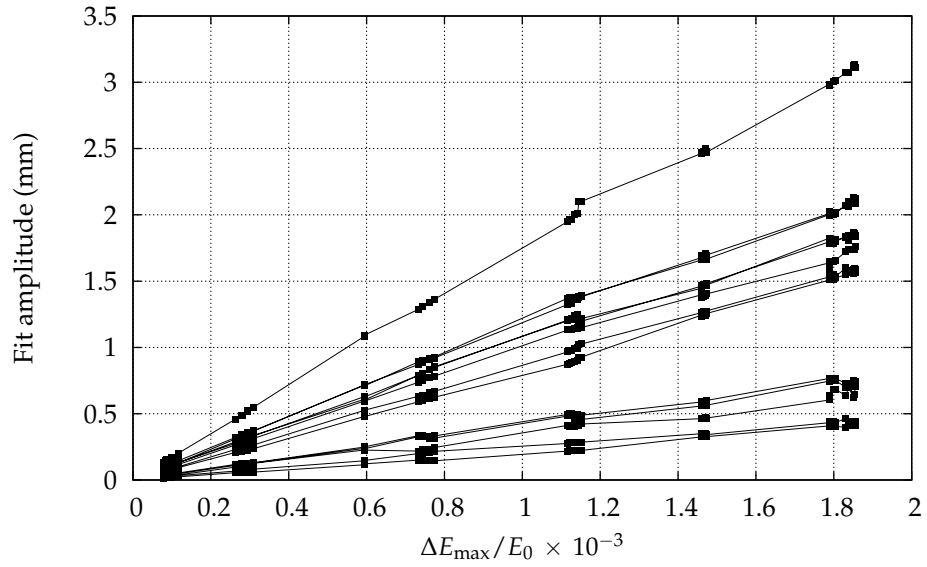
(a) Fit amplitude vs. drive amplitude
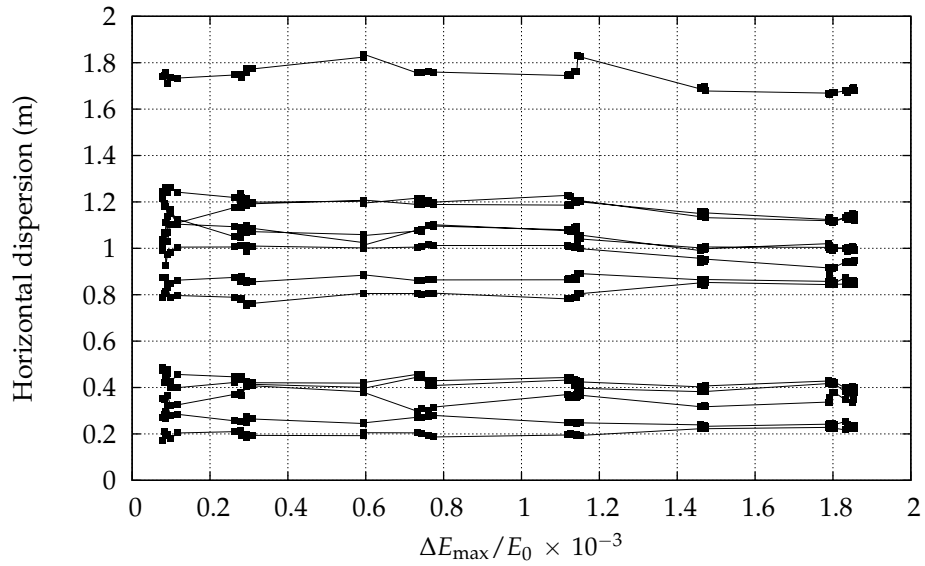
(b) Horizontal dispersion vs. drive amplitude

Figure 6.6: Drive amplitude dependence in fast dispersion measurement.

all detectors, this is somewhat circular, but if there were major problems at individual detectors (where η_x might be particularly large), that would be evident.

The bottom plot in Fig. 6.6.2 shows the actual measured value of η_x as a function of energy amplitude. From the plot, it doesn't appear that there are any systematic problems at higher energy, and this encourages us to explore even higher energy oscillations where the small signals due to vertical dispersion will be even easier to measure.

6.7   Conclusion

The principle behind this measurement technique has been demonstrated using simulation and experiment. The results obtained at CESR are encouraging, and improvements may be expected with improved instrumentation and experience. For damping rings with multiturn measurement capabilities, such as those in the ILC, this type of measurement may prove to be a useful addition to their diagnostic tools.

Chapter 7
Conclusion

We have shown that our simulations of magnet misalignments in damping rings matches the results obtained from analytic calculations. Using those simulations, we have shown that, for nominal misalignments and beam detector resolution, we can achieve the target vertical emittance of 10 pm with at least 95% confidence.

Our simulation of other possible scenarios shows that obtaining the nominal magnet alignment is critical, but that detector resolution is more forgiving, particularly with regard to the absolute position measurement.

For the ILC damping rings, we show that our beam-based alignment method satisfies the required vertical emittance, although assumptions had to be made regarding misalignments and detector performance. Our results are similar to others using different techniques. This suggests the need to standardize all of the parameters for the ILC damping rings so that more direct comparisons of effectiveness can be made.

Our fast dispersion measurement gives results that are consistent with those obtained from the traditional measurement technique, while offering some advantages over the traditional technique. When more dedicated machine time is available with CesrTA, other methods of exciting the beam can be explored. Those methods may be more relevant for using the fast technique at the ILC.

These results show that CesrTA will be able to make important contributions to the low-emittance operation of ILC damping rings.

BIBLIOGRAPHY

[1] "The Large Hadron Collider: Conceptual design," CERN-AC-95-05-LHC.

[2] E. Eichten, I. Hinchliffe, K. D. Lane, and C. Quigg, "Super Collider Physics," *Rev. Mod. Phys.*, vol. 56, pp. 579–707, 1984.

[3] H. Murayama and M. E. Peskin, "Physics opportunities of e^+e^- linear colliders," *Annual Review of Nuclear and Particle Science*, vol. 46, p. 533.

[4] "Discovering the Quantum Universe : The Role of Particle Colliders." `http://www.interactions.org/quantumuniverse/qu2006`

[5] "International Linear Collider reference design report," ILC-REPORT-2007-001.

[6] "TESLA: The superconducting electron positron linear collider with an integrated X-ray laser laboratory. Technical design report."

[7] D. L. Rubin, "Motivation and Overview for CesrTA," CesrTA Review, July 2007. `https://wiki.lepp.cornell.edu/ilc/pub/Public/CesrTA/Proposal/WebHome/motivation.pdf`

[8] M. Pivi, R. E. Kirby, T. O. Raubenheimer, and F. Le Pimpec, "Suppressing electron cloud in future linear colliders," SLAC-PUB-11201.

[9] M. A. Palmer, "CESR Test Facility Plans," LEPP Journal Club, October 2006. `https://wiki.lepp.cornell.edu/ilc/pub/Public/CesrTA/WebHome/JournalClub_CesrTF_2006_1006.ppt`

[10] J. T. Urban, G. Dugan, and M. A. Palmer, "Optimization of CESR-c superferric wiggler for the International Linear Collider damping rings," prepared for European Particle Accelerator Conference (EPAC 06), Edinburgh, Scotland, 26-30 Jun 2006.

[11] H. Wiedemann, *Particle Accelerator Physics I.* Springer, 1999.

[12] M. Sands, "The physics of electron storage rings: An introduction," 1970, SLAC-0121.

[13] M. A. Palmer, "Emittance reach for operating CESR as a damping ring test facility." `https://wiki.lepp.cornell.edu/ilc/pub/Public/CesrTA/WebHome/emittance_memo.pdf`

[14] G. H. Hoffstaetter, private communication.

[15] T. Raubenheimer, "The generation and acceleration of low emittance flat beams for future linear colliders," 1991, SLAC-0387.

[16] A. Wolski and W. Decking, "Comparison of emittance tuning simulations in the NLC and TESLA damping rings," 2002, DESY-TESLA-2002-10.

[17] S. Chapman, SurveySummary.xls.

[18] R. Holtzapple, R. Eshelman, D. Rice, G. Rouse, and A. Tamakuwala, "Leveling of the quadrupole magnets in the Cornell Electron-Positron Storage Ring," 1999, CBN-99-25.

[19] S. Chapman, private communication.

[20] *Machine Studies January 31, 2006*.

[21] W. H. Press, S. A. Teukolsky, W. T. Vetterling, and B. P. Flannery, *Numerical Recipes in Fortran 90*, 2nd ed. Cambridge University Press, 1996.

[22] D. L. Hartill, private communication.

[23] D. L. Rubin, private communication.

[24] P. P. Bagley and D. L. Rubin, "Correction of transverse coupling in a storage ring," 1989, from Proc. of 1989 IEEE Particle Accelerator Conf., Chicago, IL, Mar 20-23, 1989.

[25] A. Xiao and L. Emery, "Characterization of a 6-km damping ring for the International Linear Collider," to appear in the proceedings of Particle Accelerator Conference (PAC 05), Knoxville, Tennessee, 16-20 May 2005.

[26] *ILC damping ring lattice file*.

[27] K. Panagiotidis and A. Wolski, "Alignment sensitivities in the ILC damping rings," proceedings of PAC 2007, Albuquerque, New Mexico, Jun 2007.

[28] M. Woodley *et al.*, "Beam based alignment at the KEK-ATF damping ring," presented at 9th European Particle Accelerator Conference (EPAC 2004), Lucerne, Switzerland, 5-9 Jul 2004.

[29] J. Safranek, "Experimental determination of storage ring optics using orbit response measurements," *Nuclear Instruments and Methods in Physics Research A*, vol. 388, pp. 27–36, 1997.

[30] J. Jones, "Emittance tuning simulations in the ILC damping rings," Presentation at ILCDR07, August 2007.

[31] K. Kubo *et al.*, "Beam tuning for low emittance in kek-atf damping ring," prepared for 7th European Particle Accelerator Conference (EPAC 2000), Vienna, Austria, 26-30 Jun 2000.

[32] *Machine studies (May 30, 2006).*

[33] *Machine studies (November 7, 2006).*

[34] *Machine studies (April 24, 2007).*

[35] *Machine studies (May 7, 2007).*